


# Collisional evolution of the trans-Neptunian region in an early dynamical instability scenario

Paula G. Benavidez <sup>1,2</sup>★, Adriano Campo Bagatin,<sup>1,2</sup> Jacob Curry,<sup>1,3</sup> Álvaro Álvarez-Candal <sup>2,4</sup>  
and Jean-Baptiste Vincent <sup>5</sup>

<sup>1</sup>Departamento de Física, Ingeniería de Sistemas y Teoría de la Señal, Escuela Politécnica Superior, Universidad de Alicante, E-03690 Sant Vicent del Raspeig (Alicante), Spain

<sup>2</sup>Instituto de Física Aplicada a las Ciencias y la Tecnologías, Universidad de Alicante, E-03690 Sant Vicent del Raspeig (Alicante), Spain

<sup>3</sup>University of Surrey, Guildford, Surrey GU2 7XH, UK

<sup>4</sup>Instituto de Astrofísica de Andalucía–CSIC, E-18080 Granada, Spain

<sup>5</sup>DLR Institute of Planetary Research, D-12489 Berlin, Germany

Accepted 2022 May 30. Received 2022 May 25; in original form 2021 June 22

## ABSTRACT

Any early or late dynamical instability in the outer Solar system should have left their footprint on the trans-Neptunian object (TNO) populations. Here, we study the collisional and dynamical evolution of such populations numerically by an updated version of ALICANDEP, which suitably takes into account the onset of an early dynamical instability. Key parameters for collisional and dynamical evolution are chosen to match results with current observables. The new model (ALICANDEP-22) considers an original region located between 22 and 30 au, containing 20–30  $M_{\oplus}$  from which bodies are either dynamically ejected from the region or implanted into the current plutinos and hot classical trans-Neptunian belt. An *in situ* population of objects is also present since the beginning, corresponding to the current cold-classical population. Collisional and dynamical evolution is allowed starting from initial conditions accounting for streaming instability models and observational constraints. ALICANDEP-22 successfully reproduces observational constraints as well as the shape of the size-frequency distribution expected for the Trojan population. The model concludes that Arrokoth is likely a primordial body but cannot be conclusive on the origin of comet 67P/Churyumov–Gerasimenko. The current presence of bodies larger than Pluto in the outer TNO population – waiting to be discovered – is compatible with the initial distributions that allow the model to match current constraints.

**Key words:** Kuiper belt objects: general – planet–disc interactions – methods: numerical – minor planets, asteroids: general.

## 1 INTRODUCTION

Around 2005, a body of scientific work set up a suitable framework for explaining the giant planets’ current orbits and the dynamical state of small body populations in the Solar system. This successful framework, referred to as the ‘Nice model’, is based on the hypothesis that a giant planet dynamical instability happened hundreds of Myr after planet formation (Gomes et al. 2005). Such instability is also known as the late heavy bombardment (LHB), due to the intensive cratering period that took place on the Earth–Moon system. The Nice model explains the main dynamical mechanisms that caused part of the mass depletion of the trans-Neptunian region, the current orbits of the giant planets, and other details of the structure of the Solar system (Gomes et al. 2005; Tsiganis et al. 2005; Morbidelli et al. 2005; Levison et al. 2008). Fifteen years after the emergence of that model, the beginning, the end, and how long the LHB lasted are under discussion, as is the mechanism that triggered it (Bottke & Norman 2017; Nesvorný 2018; de Sousa et al. 2020). The critical point causing this debate is the understanding of lunar bombardment in the first Gy of the Solar system evolution (Morbidelli et al. 2018) and

its relation with the dynamical instability of giant planets. The best understood mechanism is the dynamical interaction between the giant planets and an outer disc of planetesimals (Fernandez & Ip 1984). The possibility that it was self-triggered by the giant planets themselves has also been investigated by de Sousa et al. (2020). It is worth mentioning that depending on the planets outer disc initial conditions, the instability could happen early or late. This debate shows that understanding which mechanisms explain (or better constrain) the origin of the dynamical instability is a complex problem.

Different authors have identified dynamical populations in the trans-Neptunian belt (hereafter, TB) during the past two decades. They typically follow a set of definitions originally outlined by Gladman, Marsden & Vanlaerhoven (2008). One region contains objects not usually considered to be TNOs, but that are considered to be originally trans-Neptunian. Such bodies are the Centaurs and the Jupiter Family Comets (JFCs), which orbits have been altered over time by interaction with Neptune and Jupiter. Several dynamical regions have been identified in the TB, as explained by Petit et al. (2011). There are objects in mean-motion resonance with Neptune of which the 3:2 (plutinos) and the 2:1 resonance are the most populated. Objects in the main classical belt (MCB) (with semimajor axes between the 3:2 and 2:1 resonances with Neptune) are further divided into dynamically hot and cold (Gladman et al. 2008), which

\* E-mail: paula.benavidez@ua.es

can – at first sight – be discriminated by their inclination. Objects with inclination above  $5^\circ$  are considered as dynamically ‘hot’ (hereafter HC for Hot Classical), whereas objects below such inclination are considered as dynamically ‘cold’ and are usually called Cold Classical (CC) objects.

It is widely accepted that the dynamical mechanism that governed the planet formation process, giving place to an early or late instability, would imprint some feature on the characteristics of the currently observed TB. Nesvorný (2015a, b) performed numerical simulations of the TB consistent with the five-planet model and a massive disc ( $15\text{--}20 M_\oplus$ ) located within 30 au from the Sun. Nesvorný (2015b) found that the inclination distribution of both dynamically hot populations and plutinos may be related to the time-scale of Neptune’s migration. To reach the current inclination of these populations, Neptune should have migrated slowly ( $\tau \geq 10$  Myr) and over a long-range ( $a < 25$  au). Otherwise, models with  $\tau < 10$  Myr do not match the observed inclination distribution because there is not enough time for dynamical processes to increase inclinations. Some circumstantial evidence favouring early instability came from the existence of the large Patroclus–Menoetius Jupiter Trojan binary system (Grav et al. 2011; Buie et al. 2015). Nesvorný (2018) argues that a very early (less than 100 Myr) migration of the Solar system planets would explain the Jupiter Trojan binary system survival. This binary system is believed to have been captured from a cold trans-Neptunian disc (Nesvorný, Vokrouhlický & Morbidelli 2013). Nesvorný et al. (2018) argue that delaying the planet migration to  $\sim 500\text{--}700$  Myr (Gomes et al. 2005) will allow so much collisional grinding that would strip the binary components from one another before migration takes place.

Another outstanding problem regarding migration models and the implantation process is overpopulated resonances. This problem arises because such models tend to capture more bodies in the 3:2 mean-motion resonance with Neptune than those caught as HC (Hahn & Malhotra 2005; Levison et al. 2008; Nesvorný 2015b). However, observations suggest the opposite. There seems to be  $\sim 2\text{--}4$  times more HC bodies than plutinos (Gladman et al. 2012; Adams et al. 2014). Nesvorný & Vokrouhlický (2016) propose to solve this problem by assuming that Neptune’s migration was *grainy*. *Grainy* migration means that the planetesimal disc contained 1000–4000 bodies as massive as Pluto, representing 10–40 per cent of the original disc mass, and the remaining mass is mostly in 100 km class bodies.

During the last decade, the idea that the CC population was formed locally in the outer belt has gained increasing consensus (Batygin, Brown & Fraser 2011; Wolff, Dawson & Murray-Clay 2012). For the sake of truth, it is worth mentioning that discrepancy on such an origin is still present under different arguments (e.g. Dawson & Murray-Clay 2012; Morbidelli, Gaspar & Nesvorný 2014; Gomes 2021).

The trans-Neptunian population did not only undergo dynamical evolution; it was also affected by collisional evolution. It is well known that collisional evolution was responsible for shaping the size-frequency distribution (SFD) of the TNO populations of small-size bodies, whereas dynamical effects (such as population depletion) are not size dependent. Benavidez & Campo Bagatin (2009, hereinafter BCB09) developed a three-zone model to study TNOs collisional evolution, characterizing each dynamical population by their orbital parameters, semimajor axis ( $a$ ), eccentricity ( $e$ ), and inclination ( $i$ ), also allowing populations in different zones to undergo partial collisional interaction. Campo Bagatin & Benavidez (2012, hereinafter CBB12) developed ALICANDEP (Asteroid-Like Collisional AND Dynamical Evolution Package). This package handles collisional evolution as in BCB09 and includes migration and excitation of

populations as well as statistical dynamical depletion according to the Nice model indications and requirements.

More recently, Nesvorný & Vokrouhlický (2019) studied trans-Neptunian binaries’ collisional and dynamical survival using a rounded shape for the initial SFD, obtained from hydrodynamical simulations of streaming instability (Simon et al. 2016, 2017). They showed that size distribution could have evolved collisionally to match the SFD of the hot population and Jupiter’s Trojans.

In summary, the currently accepted scenario states that the primordial disc extended from about 22 to 30 au from the Sun, with a sharp edge. During dynamical instability, this disc was strongly depleted by the influence of Neptune, some bodies were implanted in the plutinos region and others would end up as HC. The presence of some initial mass beyond 30 au is compatible with a distribution of mass in which the CC belt would have formed. Most recent literature suggests two different size distributions for the primordial disc population informed by streaming instability models (Nesvorný & Vokrouhlický 2016, 2019), contrasting with traditionally assumed power laws. Nevertheless, there is no consensus on the strength parameters that govern the response to collisions in the TB. For instance, Morbidelli et al. (2021, hereinafter M21) revised previous estimation by Singer et al. (2019) by connecting the crater record on Charon with that on Arrokoth and with the dust measurements from the inspected dust count by the New Horizons space mission (NASA). It turns out that the SFD is shallow below 2 km, but not as shallow as claimed by Singer et al. (2019), and the shallow branch of the SFD extends down to some 30 m, before steepening up again to match the dust abundance constraint. M21 claims that this SFD is consistent with collisional equilibrium, provided that the transition from the strength regime to the gravity regime occurs at  $D \sim 30$  m, in contrast to the minimum transition diameter of 100–200 m estimated by Benz & Asphaug (1999) and Leinhardt & Stewart (2009) for ice bodies.

The main purpose of this work is to systematically study how the SFDs proposed in the literature respond to dynamical and collisional evolution in the framework of an early evolution. Therefore, we modified the ALICANDEP code to include the main features of the new proposed evolution scenarios. Equipped with ALICANDEP-22, we have performed about numerical simulations systematically exploring different scaling laws and varying the onset time of dynamical instability ( $t_i$ ). To select the best scenarios, we compare our results with the following observable constraints: the number of bodies larger than 100 km for all dynamical populations, the number of dwarf planets, the lack of large bodies in the cold population, and the estimated SFD slope for HC and CC objects. Section 1.1 describes each of these constraints.

Once the main purpose is reached, we apply our model to the problem of the origin of comet 67P/Churyumov–Gerasimenko (hereinafter, 67P/C-G), visited by the Rosetta space mission (ESA) in the past decade and to the origin of the TNO 486958 Arrokoth, flown-by in early 2019 by the New Horizons mission. A debate arose about their primordial against evolutionary genesis (Sierks et al. 2015; Jutzi et al. 2017; Spencer et al. 2020) to which we contribute with this study.

The following subsections briefly summarize the current observables that constrain this study, and the main features of 67P/C-G and Arrokoth are introduced.

## 1.1 Current observables in the TB

Any reliable evolution model should match most of the characteristics of the observable populations. Here, we compile the main

features of the current TB populations to which we will compare the results obtained by our model.

Number of bodies larger than 100 km: As the large end of the size distribution is well characterized by observational evidence, we rely on the estimation provided by the Canada-France Ecliptic Plane Survey (CFEPS) simulator and the Outer Solar System Origins Survey (OSSOS), for the trans-Neptunian populations (Kavelaars et al. 2009; Bannister et al. 2018). Gladman et al. (2012) estimated that the Plutinos population has  $13_{-5}^{+6} \times 10^3$  objects with  $D > 100$  km; more recently Alexandersen et al. (2016) and Volk et al. (2016) estimated that it has  $9000 \pm 3000$  and  $8000_{-4000}^{+4700}$  bodies ( $D > 100$  km), respectively. Thus, we consider our results to be in good agreement with the plutinos population when they fall in the intersection between these estimated ranges. Petit et al. (2011) estimated that there are  $35_{-7}^{+8} \times 10^3$  HC bodies larger than 100 km, whereas the CC is as numerous as  $95_{-16}^{+18} \times 10^3$ . However, recent estimations from OSSOS have reduced the estimation for the latter population to about  $15 \times 10^3$  bodies (Nesvorný et al. 2020; Kavelaars et al. 2021). Due to the large difference between both estimates, we will use the most recent estimate as a constraint for the CC belt.

Number of dwarf planets: Currently, four dwarf planets have been discovered in the trans-Neptunian belt. Pluto ( $D = 2380$  km) in the plutinos population, Makemake and Haumea (both  $\sim 1400$  km) in the HC belt, and Eris in the detached classical belt (although this last population is outside the scope of this work).

Lack of large bodies in the cold population: Here, we consider the cold population of the MCB as the stirred and kernel populations together (Petit et al. 2011), both having low inclination. The lack of bodies larger than 400 km has been confirmed by Kavelaars et al. (2021), suggesting that the accretion process was halted at such size in this region (Nesvorný 2018).

Features in the SFD: The estimated SFD – usually represented by  $dN/dD \propto D^{-q}$  – are based on the absolute magnitude distribution. This has a differential form,  $dN/dH \propto 10^{\alpha H}$ , where  $dN/dH$  is the number of objects per  $dH$ -mag interval, and  $\alpha$  is the exponent of the distribution. The slope index  $q$  in the size distribution is determined from the relation  $q = 5\alpha + 1$ . Volk et al. (2016) found that a single slope  $\alpha = 0.9_{-0.4}^{+0.2}$  ( $q = 5.5_{-2.4}^{+1.2}$ ) could be acceptable for modelling the plutinos population, opposite to a transition in the SFD suggested by Alexandersen et al. (2016). Petit et al. (2011) provided estimation for the CC and HC components of the MCB. They claim that different slopes of the luminosity function ( $\alpha$ ) for cold and hot population,  $\alpha_{CC} = 1.2_{-0.3}^{+1.2}$  and  $\alpha_{HC} = 0.8_{-0.1}^{+0.3}$ , are needed to improve the data fit. Then, the differential SFD slope indexes are determined to be  $q_{CC} = 7$  and  $q_{HC} = 5$ . Later, Fraser et al. (2014) estimated the slope of the size distributions by also splitting the TB population into cold and hot subpopulations being  $q_{CC} = 8.2 \pm 1.5$  and  $q_{HC} = 5.3_{-1}^{+0.4}$  for bodies larger than  $\sim 100$  km, respectively. They also pointed out that both populations share a similar slope ( $\sim 2$ ) for smaller bodies. Their fits also allow them to estimate the mass in the CC and HC populations as  $M_{CC} = 3 \times 10^{-4} M_{\oplus}$  and  $M_{HC} = 0.01 M_{\oplus}$ , respectively. Recently, Kavelaars et al. (2021) found that the shape of the CC population  $H_r$  distribution is inconsistent with a two-component power-law fit, rather revealing an exponential cut-off at large sizes. Note that tapered power laws are becoming the favoured representation in streaming instability models of planetesimal formation.

## 1.2 Main features of 67P/C-G and Arrokoth

The Jupiter-family comet 67P/C-G has been studied in detail by the *Rosetta* (ESA) rendez-vous mission (Sierks et al. 2015). Jorda

et al. (2016) estimated the size of the two individual lobes to be  $4.10 \times 3.52 \times 1.63$  km and  $2.5 \times 2.14 \times 1.64$  km for the larger and smaller lobes, respectively. The derived combined volume of 67P/C-G is  $18.8 \pm 0.3$  km<sup>3</sup>, which together with estimated mass, gives a bulk density of  $532 \pm 7$  kg m<sup>-3</sup>. In light of the outstanding images and the high precision measurements provided by the *Rosetta* mission, the debate on whether that — and other — comets are pristine planetesimals or collisionally evolved objects resurfaced. In this sense, Brassier & Morbidelli (2013) suggested that both the Scattered disc and the Oort Cloud comets could be formed together in the primordial trans-Neptunian disc in the framework of the original Nice Model. Later, Morbidelli & Rickman (2015) revisited this issue in the framework of both scenarios, early and late giant planet instability. The latter work suggests that Jupiter family comets and Oort Cloud comets should be fragments of originally larger bodies in the late scenario. However, in an early giant planet instability scenario dispersing the primordial disc, they found that the collisional evolution of comet-size bodies in the scattered disc would have been less severe.

Regarding the trans-Neptunian object Arrokoth, it was found to be a contact binary by the New Horizons (NASA) mission. According to Spencer et al. (2020), both lobes are roughly ellipsoidal, with sizes  $20.6 \times 19.9 \times 9.4$  km and  $15.4 \times 13.8 \times 9.8$  km, respectively. They estimated its equivalent size, that is, the diameter corresponding to an equal volume sphere to be  $18.3 \pm 1.2$  km. The orbital parameters determined for Arrokoth placed it clearly as a member of the cold classical belt (Porter et al. 2018), particularly into the kernel sub-population defined by Petit et al. (2011). Spencer et al. (2020) determined a low crater density, compatible with a surface age of  $>4$  Gy. These authors suggest that Arrokoth could be a direct product of the accretion process rather than a collisional fragment.

This paper is structured as follows. After this introduction, Section 2 describes the methodology of the study and the main features of ALICANDEP-22. In Section 3, results are presented and compared to observables. Also, an analysis of the odds for a primordial or evolutive origin of 67P/C-G and Arrokoth is carried out. In Section 4, a discussion of results and conclusions are presented.

## 2 METHODOLOGY

We study the collisional and dynamical evolution of the trans-Neptunian populations using numerical simulations based on the package ALICANDEP, thoroughly described in CBB12. Here, we updated the model (to ALICANDEP-22), and we adopted a simple scheme to include the possibility of considering an early dynamical excitation scenario under the current framework. This model includes statistical elimination and implantation of bodies from an inner disc to current TB regions, modelling dynamical effects present in the Nice model (CBB12) and its current interpretation. Initially, most mass is concentrated in an inner disc ranging from just outside Neptune's initial orbit –from about 22 to 30 au and a small amount of mass is initially located between 42 and 47 au, to simulate the *in situ* formation of the cold classical disc. The inner disc evolves not only collisionally but also dynamically. Such an inner disc undergoes collisional evolution and simultaneous dynamical excitation and depletion in an initially cold massive disc. Dynamical excitation during the instability of the giant planet triggers smooth dynamical elimination of mass during the pre-instability phase, which is handled statistically. Lastly, further elimination and implantation of planetesimals to the outer region take place. Such region is modelled as three



zones, accounting for the plutinos, the CC and HC populations. A more detailed explanation is given in Section 2.2.

The main features of the model are (i) Numerical solution, at each time step, by an Euler method, of a set of  $N$  differential equations representing the total populations as well as the number of gravitational aggregates at any size interval. Such equations include terms related to the production and elimination of objects due to impacts and dynamical effects. (ii) Calculation of the number of fragments produced in collisions between bodies belonging to any size interval according to available scaling laws for fragmentation and cratering. Two kinds of objects are considered (monolithic and gravitational aggregates), for which different responses to collisions are considered. (iii) Overlapping between zones is allowed so that interaction in terms of collisions between border bodies is accounted for.

The model evolves over time the collisional interaction and dynamical depletion of objects in discrete logarithmic size bins, whose central values span from 7 cm to 6000 km in diameter so that two adjacent bins always scale a factor 2 in mass ( $\sim 1.26$  in size). Furthermore, ALICANDEP-22 is able to follow both *resident* and *primordial* bodies in initially populated zones. We define *resident* bodies as those that remain all the time in their initial zone. The resident population is therefore not increased by external migration but may evolve under mutual collisions. In contrast, *primordial* bodies do not suffer any shattering collision but can undergo collisions below the shattering threshold, such as cratering and re-shaping.

The model has also been improved to study in detail the evolution of populations corresponding to objects of special interest, as is the case of Arrokoth and comet 67P/C-G, once belonging to the TB. We can track the evolution of TNOs corresponding size ranges and evaluate the abundance of gravitational aggregates (GA, as defined in Section 2.1), resident and primordial bodies.

## 2.1 Collisional model

The fragmentation algorithm is based on the fragmentation and re-accumulation model by Petit & Farinella (1993), and later updates based on available experimental data, numerical, and theoretical studies. This part of the package computes the number of fragments produced in any possible collision between objects belonging to different size (mass) bins. According to available scaling laws, different algorithms for shattering and cratering events are used. We assumed the following scaling laws to perform our simulations:

(i) SL1: Scaling law for ice introduced by Benz & Asphaug (1999, hereafter BA99) derived from smooth particle hydrocode (SPH) numerical simulations. This scaling law contains two terms corresponding to the strength and gravity regimes to scale the disruption shattering threshold from laboratory experimental conditions for shattering to small Solar system body size:

$$Q_D^* = Q_0 \left( \frac{R_b}{1 \text{ cm}} \right)^c + B \rho \left( \frac{R_b}{1 \text{ cm}} \right)^d \quad (1)$$

where  $Q_D^*$  is defined as the threshold energy per unit mass necessary to shatter and disperse half of the mass of the parent body.  $R_b$  is the radius of the target,  $Q_0$ ,  $c$ ,  $d$ , and  $B$  are parameters corresponding to different material characteristics and relative impact speeds of target bodies with density  $\rho$ , which is averaged to  $1000 \text{ kg m}^{-3}$  for icy bodies. For involved parameters, we consider the corresponding values for ice, as given by the authors:  $Q_0 = 1.6 \times 10^3 \text{ J kg}^{-1}$ ,  $B = 1.2 \times 10^{-7} \text{ J m}^3 \text{ kg}^{-2}$ ,  $c = -0.39$ , and  $d = 1.26$  for impact speed of

$3 \text{ km s}^{-1}$ .  $Q_0 = 7 \times 10^3 \text{ J kg}^{-1}$ ,  $B = 2.1 \times 10^{-7} \text{ J m}^3 \text{ kg}^{-2}$ ,  $c = -0.45$ , and  $d = 1.19$  for impact speed of  $0.5 \text{ km s}^{-1}$ .

(ii) SL2: This is the same as SL1, but scaling  $Q_D^*$  down by a factor of 0.1. We chose this scaling factor in agreement with previous studies (Nesvorný & Vokrouhlický 2016).

(iii) SL3: This is the same as SL1, but scaling the  $Q_D^*$  down by a factor of 0.06 and shifting the minimum of  $Q_D^*$  to 30 m. We chose this scaling law following Morbidelli et al. (2021) results that suggest that the transition from the strength regime to the gravity regime may occur at 30 m.

(iv) SL4: Scaling law by Leinhardt & Stewart (2009) and Leinhardt & Stewart (2012). They derived alternative scaling laws for icy bodies based on a different numerical method (CTH; a shock wave physics software package), leading to shattering critical specific energies grossly one order of magnitude smaller than BA99. The functional form of LS09 scaling law is the same as BA99, but their recommended parameter values are different:  $Q_0 = 20 \text{ J kg}^{-1}$ ,  $B = 3.5 \times 10^{-6} \text{ J m}^{-3} \text{ kg}^{-2}$ .

In addition to that, whatever the assumed scaling law is, we reduce  $Q_D$  by a factor of 10 in the case of gravitational aggregates to account for the fact that such bodies are harder to disperse, according to available modelling (see e.g. Campo Bagatin, Petit & Farinella 2001 and references therein). Other scaling laws have been suggested in the literature, but we prefer to restrict to the four mentioned because they reasonably represent distinctive body strengths. Fig. 1 shows a comparison of the four scaling laws considered. SL1 makes small bodies about 100 times harder than SL4, whereas large bodies are only about a factor 10 harder. SL3 makes small bodies as weak as SL4 (LS09), but large bodies as strong as SL1 (BA99). Therefore, using these scaling laws allows us to explore the effect of collisions under quite different impact response.

The Petit & Farinella (1993) algorithm allows for the derivation of the threshold specific energy for shattering ( $Q_S^*$ ) from the threshold specific energy for disruption ( $Q_D^*$ ), given by the considered scaling laws. This allows us to discriminate between conditions for shattering and calculate the amount of mass that will be re-accumulated due to self-gravity, and keep track of GA subpopulation. It is worth mentioning that – according to the definition given by Campo Bagatin et al. (2001) – after each collision, a body is classified as a GA if the mass of the largest fragment produced by shattering is less than half the mass of the whole re-accumulated object after the collision. The populations of GA of each size are tracked along with the whole evolution. Such populations are affected by the disruption of existing GA and by the formation of new re-accumulated bodies belonging to the corresponding size bins.

## 2.2 Boundary conditions and time evolution

ALICANDEP-22 handles the evolution of four zones (instead of three zones in previous version): an Inner Zone evolves collisionally without interaction with other zones and three outer interacting zones. Each zone is calculated as a geometric toroid with rectangular section (CBB12) so that (see Table 1):

- Inner Zone :  $a_{0, \text{inn}}(1 - e_0) < i < a_{0, \text{out}}(1 + e_0)$ ;
- Zone 1 :  $a_1(1 - e_1) < r_1 < a_2(1 + e_1)$ ;
- Zone 2 :  $a_2(1 - e_2) < r_2 < a_3(1 + e_2)$ ;
- Zone 3 :  $a_1(1 - e_3) < r_3 < a_3(1 + e_3)$ .

The range and location of the Inner Zone are constrained by the initial conditions of dynamical models, which usually assume an inner primordial cold disc from  $\sim 22$  to 30 au. The size and location of the three outer zones are instead defined by the orbital

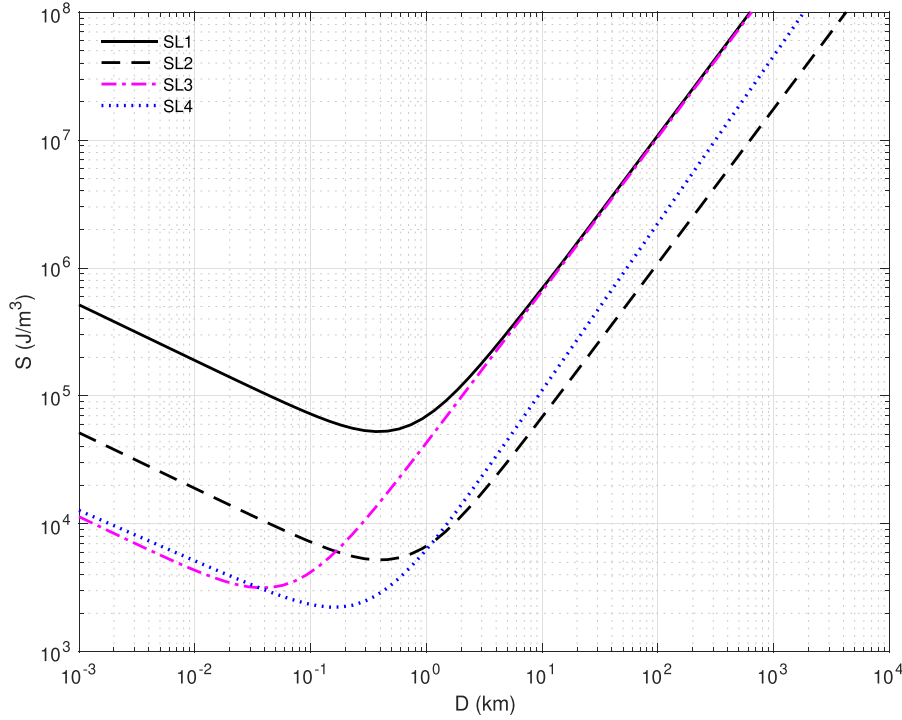


**Figure 1.** Scaling laws used in this study corresponding to SL1 Benz & Asphaug (1999) for ice bodies; SL2, same as SL1, but scaled down by a factor 0.1; SL3, same than SL1, but scaling  $Q_D^*$  down by a factor of 0.06 and shifting the minimum to 30 m; SL4, scaling law by Leinhardt & Stewart (2009) and Leinhardt & Stewart (2012).

**Table 1.** Orbital element boundary values for dynamical zones (subindex, 0, 1, 2, 3) and for each dynamical phase.

| Phase                        | $a_0$ (au) | $a_1$ (au) | $a_2$ (au) | $a_3$ (au) | $e_0$   | $e_1$ | $e_2$ | $e_3$ | $i_0$ (°) | $i_1$ (°) | $i_2$ (°) | $i_3$ (°) |
|------------------------------|------------|------------|------------|------------|---------|-------|-------|-------|-----------|-----------|-----------|-----------|
| 1 ( $0, t_i$ )               | 22–30      | 38         | 42         | 47         | 0.1–0.2 | –     | 0.05  | –     | 10–20     | –         | 5–10      | –         |
| 2 ( $t_i, t_i + \Delta t$ )  | 22–30      | 38         | 42         | 47         | 0.2     | 0.18  | 0.05  | 0.2   | 20        | 20        | 10        | 20        |
| 3 ( $t_i + \Delta t, 4500$ ) | –          | 38         | 42         | 47         | –       | 0.18  | 0.05  | 0.2   | –         | 20        | 10        | 20        |

elements observed for each dynamical population in the current trans-Neptunian region. Here, we assume that the three outer zones do not undergo dynamical alteration since the bodies are implanted into them. At the beginning of evolution, most of the initial mass ( $M_0$ ) was concentrated in the Inner Zone and a small portion was situated in Zone 2. Zones 1 and 3 are initially empty.

Evolution takes place at different phases, characterized by values for eccentricity, inclination, and semimajor axes in each zone, as summarized in Table 1:

(i) *PHASE 1*: From 0 to  $t_i$ . This is the pre-instability phase. The Inner Zone undergoes dynamical excitation and partial mass-loss, and mainly collisional evolution takes place. The Inner Zone slowly starts losing mass due to smooth dynamical interactions, reaching the instability time with  $\sim 20 M_\oplus$ .

(ii) *PHASE 2*: From  $t_i$  to  $t_i + \Delta t$ . This is the dynamical instability phase itself. The inner disc reaches this phase partially excited, strong depletion due to further dynamical interaction with Neptune, and implantation of bodies to Zones 1 and 3 take place.

(iii) *PHASE 3*: From  $t_i + \Delta t$  Myr to the end of evolution (4500 Myr). Here, the Inner Zone is empty, and the three outer zones reach a quiet period, leading to the current stable situation.

We performed systematic simulations assuming  $t_i = 5, 10,$  and  $30$  Myr and  $\Delta t = 10$  Myr, but we also tested evolution with  $t_i = 10$

and  $\Delta t = 100$  Myr, and  $t_i = 10$  and  $\Delta t = 30$  Myr in order to compare with cases C1 and C2 from Nesvorný & Vokrouhlický (2016). Our modelled outer region follows the dynamical classification of Petit et al. (2011):

- (i) Zone 1 makes up the portion of the belt that is closer to Neptune than the 3:2 resonance, including the plutinos population.
- (ii) Zone 2 corresponds to the CC belt.
- (iii) Zone 3 represents the HC belt population.

The overall collisional and dynamical time evolution for each bin is therefore fully described by a system of  $n$  non-linear, second-order differential equations.

Equation (2) for the Inner Zone 0, and (3) for zones 1, 2, and 3, give the change in time of the number of bodies ( $N$ ) in each size bin ( $k$ ), in a given dynamical phase  $\mathbf{p}$  ( $\mathbf{p} = 1, 2, 3$ ):

$$\frac{dN_0(k)}{dt} = \sum_i^n \sum_j^i \left\{ \sum_l^m [f_{ijkl} p(V_l) s_{i,j,l}] \right\} \times \frac{(N_0(i) - \delta_{ij}) N_0(j)}{1 + \delta_{ij}} - \alpha_p N_0(k) - \beta_{pz} N_0(k), \quad (2)$$

$$\begin{aligned} \frac{dN_z(k)}{dt} = & \sum_i^n \sum_j^i \left\{ \sum_l^m [f_{ijkl} p(V_l) s_{i,j,l}] \right\} \\ & \times \frac{(N_z(i) - \delta_{ij}) N_z(j)}{1 + \delta_{ij}} (1 + \gamma_x + \gamma_y) \\ & + [\beta_{pz} N_0(k)], \end{aligned} \quad (3)$$

where  $n$  and  $m$  are the total number of size and speed bins, respectively. The projectile index  $j$  ranges from 1 to  $i$ , due to symmetry of the  $f_{ijkl}$  array, which is the output of the fragmentation algorithm;  $p(V_l)$  is the probability corresponding to the  $l$ th generic discrete interval of the relative speed distribution centred at  $v_l$ , and  $s_{i,j,l}$  is the collisional cross-section for objects of size  $D_i$  and  $D_j$  at speed  $v_l$ .  $s_{i,j,l} = \frac{1}{4} P_{\text{int}}(D_i + D_j)^2 \{1 + (V_{\text{esc}}/V_l)^2\}$ . This term includes gravitational focussing, important only for the largest bodies.  $\delta_{ij} = 1$  if  $i = j$ , and 0 otherwise.  $V_{\text{esc}} = \sqrt{\frac{8}{3} \pi \rho G R^2}$  is the escape velocity from the target body with  $\rho$  bulk density, and  $P_{\text{int}}$  is the intrinsic collisional probability (which is a function of the relative velocity, volume and orbital elements for each zone).  $\gamma_x$  and  $\gamma_y$  account for collisions between bodies in any considered dynamical zone  $z$  and those in any of the neighbouring zones  $x$  and  $y$ .

Coefficients for population reduction, feeding, and zone interaction (ranging from 0 to 1) are used in equations (2) and (3):  $\alpha_p$  and  $\beta_{pz}$  are, respectively, elimination and implantation rates per unit time, relative to the number of bodies in each bin.

$\alpha_p$  is the elimination rate in the Inner Zone (0) due to dynamical effects during phases  $p = 1$  and  $p = 2$ .  $\alpha_p = 0$  for dynamical phase 3. Notice that this fraction of bodies per unit time does not contribute to the migration of bodies to Zones 1 and 3. That is the fraction of bodies ejected from the Inner Zone to beyond zones 1, 2, and 3.

$\beta_{pz}$  is the implantation rate into zone  $z$  during phase ( $p$ ).  $\beta_{pz} \neq 0$  only for  $p = 2$  and  $z = 1, 3$ . In fact, body migration is only possible in phase 2 towards Zone 1 and 3, as Zone 2 (CC) does not receive new dwellers. This is also a negative contribution to Inner Zone (0) (equation 2), and a positive contribution to  $\frac{dN_z(k)}{dt}$  for Zone 1 and 3 (equation 3) during phase 2.

We have been tuning the value of  $\alpha_1$  until the disc mass reached about  $20 M_{\oplus}$  at the beginning of the instability, and  $\alpha_2$  until the Inner Zone is empty.  $\beta_{2z}$  is adjusted simultaneously until the final population corresponding to  $D > 100$  km achieves the expected number of bodies in each zone.

### 2.3 Initial size and mass distribution

This study considered four different initial SFDs for the primordial population in the Inner Zone. First, we consider the distribution from Nesvorný & Vokrouhlický (2016) that suggests that Neptune’s migration was grainy, requiring between 1000 and 4000 Pluto-class objects. Here, we start from the reconstructed distribution of fig. 15 for the mentioned paper that the authors normalized to a total mass of  $20 M_{\oplus}$ . Hereinafter, we will refer to this as the NV16 SFD. The reconstructed NV16 SFD contains  $21.08 M_{\oplus}$  in the whole size range (7 cm to 6000 km, including  $\sim 2000$  bodies larger than 2000 km, about 13 per cent of the initial mass. Secondly, we consider the initial distribution proposed by Nesvorný & Vokrouhlický (2019), who adopted a rounded SFD informed by planetesimal formation models. Here, we reconstructed the distribution of Fig. 9 of that paper, in which the authors indicate a total mass of  $30 M_{\oplus}$ ; from now on, we will refer to this as the NV19 SFD. Our reconstructed SFD contains  $29.66 M_{\oplus}$  in the size range considered in this work; here, less than 3 per cent of the initial mass is in Pluto-size bodies or larger. We have

also tested a more traditional SFD distribution, usually described by a broken power-law  $dN \propto D^{-q} dD$ . Cumulative size distribution is often used in the literature as  $N(> D) \propto D^{1-q}$ . Different ways of representing SFDs are summarized by O’Brien & Greenberg (2005).

Different indexes,  $q_S$  and  $q_L$ , for the broken power-law (BPL) at small and large bodies matching at some transition size  $D_b$  have been proposed in the past. The BPL that describes the initial population is

$$\begin{aligned} dN(D) & \propto D^{-q_S} dD \quad \text{if } D \leq D_b, \\ dN(D) & \propto D^{-q_L} dD \quad \text{if } D > D_b, \end{aligned} \quad (4)$$

where  $dN$  is the incremental number of bodies in the interval  $[D, D + dD]$ .  $D_b$  is the break size, and  $-q_S$  and  $-q_L$  are the slopes of the size distribution for smaller and larger sizes, respectively.

All along this work, we are making reference to the slope of the incremental distribution ( $q_S$  and  $q_L$ ), both when dealing with initial and final SFD. Nevertheless, we choose cumulative distributions in the corresponding figures to make it easier to compare the model with other authors’ results. Here, we tested two broken power laws for the initial populations, where the main difference is the number of bodies smaller than  $D_b = 100$  km.

The initial distribution slope indexes ( $q_S$ ,  $q_L$ ) used are  $(-0.5, 5)$  and  $(2, 5)$ , giving a total mass of  $25.8$  and  $31.8 M_{\oplus}$ , we refer to those as BPL1 and BPL2, respectively. Since some bodies from the Inner Zone will populate zones 1 and 3, we chose  $q_L$  according to the observed slopes of the plutinos and HC populations and kept the total mass at values comparable to the SFDs mentioned above.

Finally, to consider the *in situ* formation and subsequent evolution of the CC population, we assumed the distribution used by Nesvorný et al. (2020), which is inspired by streaming instability models. They provide the following function for the cumulative distribution, where the power law is exponentially tapered for bodies larger than  $D_0$ :

$$N(> D) = A \left( \frac{D}{D_0} \right)^f \exp \left[ - \left( \frac{D}{D_0} \right)^g \right], \quad (5)$$

The authors provide the following values for the parameters:  $A \simeq 1.3 \times 10^5$ ,  $f \simeq 0.6$ ,  $g \simeq 1.2$ , and  $D_0 \simeq 60$  km, given an initial mass of  $5 \times 10^{-3} M_{\oplus}$ . Fig. 2 compares all initial SFDs considered in this work in cumulative and differential representations.

## 3 RESULTS

We performed a large set of numerical simulations, exploring the parameter space to illustrate the consequence of the different evolution scenarios. In summary, we explored four SFDs, namely: NV16, NV19 and BPL1 and BPL2, as described in Section 2.3. For each SFD, we run our model using each of the four scaling laws described in Section 2.1. In addition, we sampled three values for the onset of dynamical instability ( $t_i = 5, 10, \text{ and } 30$  Myr) for each case, considering a nominal time duration,  $\Delta t = 10$  Myr. Furthermore, for NV16 SFD cases, we performed two extra runs:  $t_i = 10$  Myr and  $\Delta t = 30$  Myr, and  $t_i = 30$  Myr and  $\Delta = 100$  Myr. All that makes 56 runs altogether.

Here, we report the main results obtained from our numerical simulations. First, we assess all runs to select the ones with the best chance of reproducing current observables that fulfil the constraints listed in Section 1.1. Figs 3–6 show the final SFDs for all runs highlighting the critical constraints for the plutinos, HC, and CC populations. The most successful runs are listed in Table 2. Lastly, considering successful cases, we focus on discussing the primordial or eroded nature of 67P/C-G and Arrokoth, based on our model results.

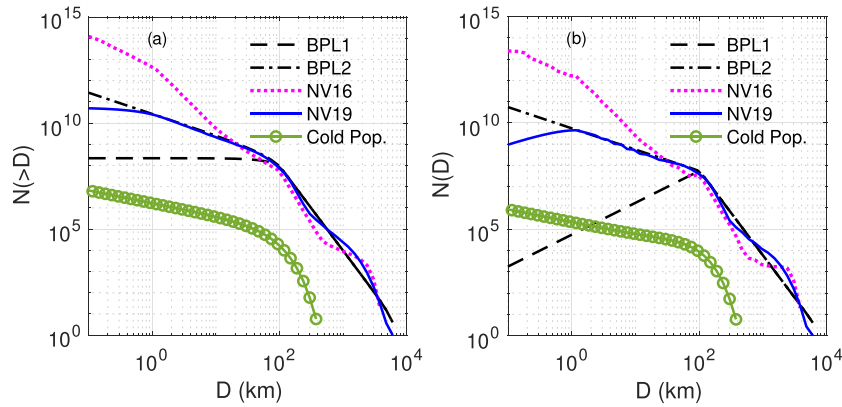


**Figure 2.** Initial size-frequency distributions, as described in Section 2.3. (a) Cumulative representation and (b) incremental representation.

### 3.1 Comparison to observables

#### 3.1.1 Number of bodies larger than 100 km.

Suitable tuning of both dynamical mass depletion and the fraction of implantation of bodies into the plutinos and HC regions allows acceptable adjustment of the number of estimated bodies larger than 100 km in each dynamical population. It is possible to eventually fulfil this condition for all evaluated SFDs, with different  $t_i$ , and scaling laws. Nevertheless, not every case satisfies the condition of ending the simulation with the expected number of dwarf planets, which leads to further selection.

#### 3.1.2 Number of dwarf planets

ALICANDEP-22 handles statistics of collisions and depletion for a small number of bodies using Poisson probability distributions. For this reason, simulations with identical initial conditions may result in a slightly different outcome for the number of large bodies. In order to improve statistical estimation, we run seven twin runs of each case providing the correct number of bodies larger than 100 km. We consider as successful cases those that meet the criteria to have a high Poisson probability of matching the expected  $N = 1$  and  $N = 2$  for the plutinos and HC population. On average, the average number of dwarf planets we found in the plutinos population and HC belt is 0.9 and 1.8, respectively.

Of the four SFDs evolved under different conditions, only NV16 and NV19 distributions allow plutinos and HC populations to receive enough large bodies from the initial inner region to end up with currently observed dwarf planets. In contrast, BPL SFDs always end the evolution with fewer dwarf planets than expected. This is mainly due to the bump in the range of large bodies ( $> 1000$  km) present in NV16 and NV19 SFDs, which favours the survival of dwarf planets. Table 2 summarizes successful cases meeting all constraints imposed by observables. In addition, the table shows the average number of dwarf planets found in each case.

Adjusting the dwarf planet population in the HC region implies – in some cases – a non-zero probability for large bodies to survive in that region. In particular, we obtain a Poisson probability of 0.83 to have at least one undiscovered body larger than 1700 km in the HC. The cases that statistically best fit the number of expected dwarf planets and minimize the probability of undiscovered dwarf planets in the HC are C2 (0.68), C4 (0.68), and C10 (0.51).

#### 3.1.3 Lack of large bodies in the cold population

Concerning the CC population, there is observational evidence of a lack of bodies with  $D > 400$  km. All of our successful simulations are consistent with such expectations as no large body of that size is in the initial population.

#### 3.1.4 Features in the SFD

Figs 3–6 show all runs combining different initial conditions and scaling laws. Any single successful case is highlighted in green in the online version; that means it is successful for all populations, in such a case, there will be one green curve for each population corresponding to that successful case. It may not be easy to figure out small differences in log-log plots; similar curves may be close to success criteria but still miss some. That is what happens for non-green curves. Many combinations of initial SFD and scaling law fail to meet the requested constraints for the population and number of dwarf planets at the end of evolution time.

Almost all collisional evolution takes place in the Inner Zone, and it lasts a relatively short period of time. Therefore, even wide differences in scaling laws do not have enough time to clearly shape final distributions according to them as collisional equilibrium is not reached. However, even such a short period of evolution is enough to essentially re-build the small body populations, but not to change the size distribution at larger sizes. For that reason, the initial distribution shape for large bodies is preserved, while any feature related to scaling laws has not enough time to show up in the final distribution.

It is generally accepted that a single power-law cannot be extended to sizes smaller than  $\sim 100$  km. In fact, even if several difficulties prevent complete and well-calibrated surveys at small sizes, there is observable indication that, at weak magnitudes, the SFD has a somewhat flat transition to the small body size with a shallow slope (Bernstein et al. 2004; Fuentes & Holman 2008; Shankman et al. 2013; Adams et al. 2014; Fraser et al. 2014).

For the successful cases indicated in Table 2, the SFD slope for bodies larger than 100 km is estimated for our three outer zones, corresponding to plutinos, HC, and CC populations. The results agree with what is estimated from observational data within uncertainties. Our estimation of  $q_L$  for the plutinos and HC belt are in the 5.8–6.2 and 5.9–6.1, respectively.

As for the CC belt, all our runs give  $q_L = 6.9$ . The large end ( $D > 100$  km) of the SFD has been calibrated by the CFEPS survey simulator (Petit et al. 2011), in which cold and hot populations seem



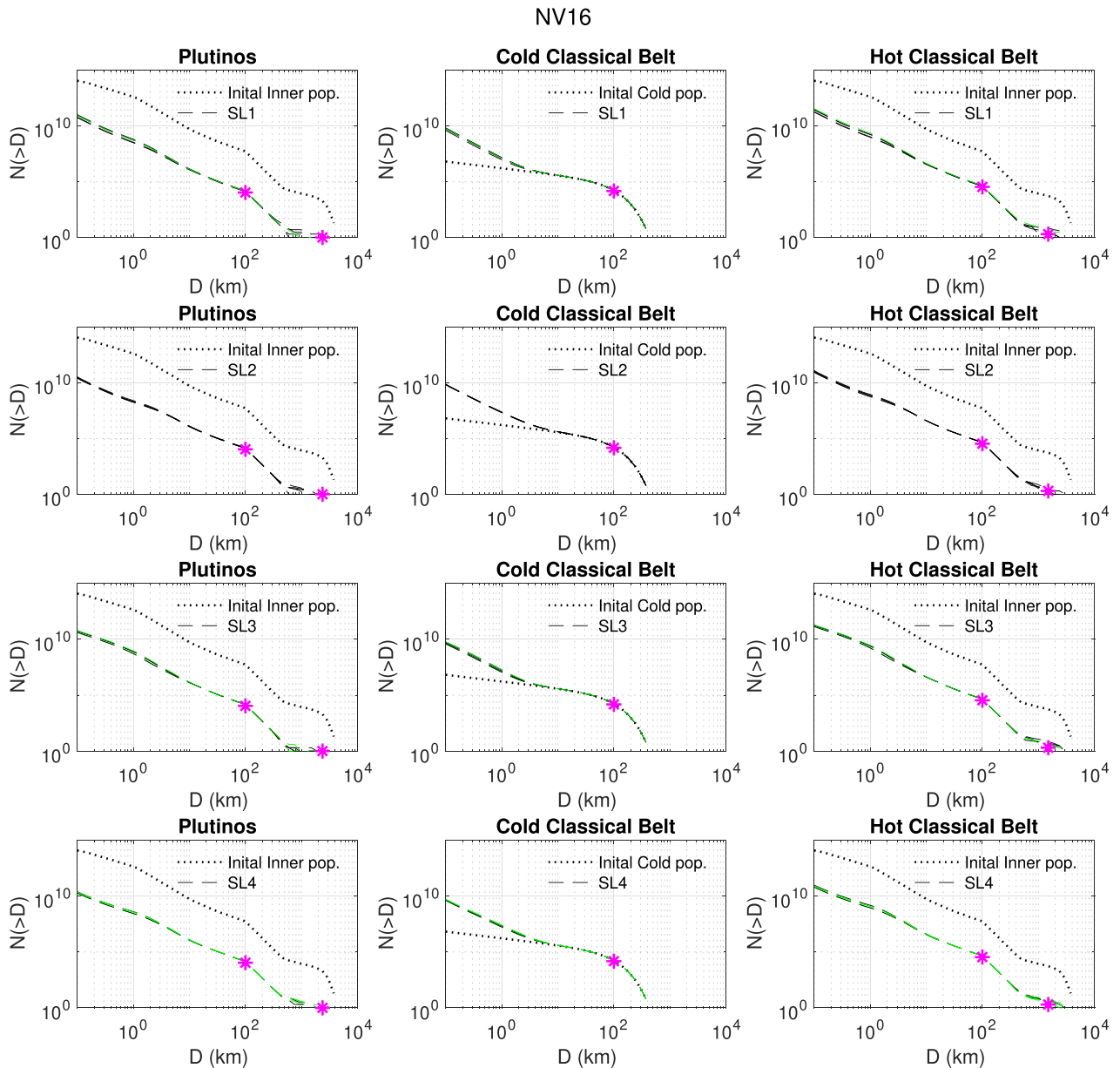


**Figure 3.** Cumulative final size-frequency distributions for Zone 1 (Plutinos), Zone 2 (CC), and Zone 3 (HCs), with initial NV16 SFD. Each plot includes all runs performed with the same scaling law, but different  $t_i$ . The magenta asterisks represent the number of bodies larger than 100 km and the number of dwarf planets as indicated in Table 2. Green dashed lines correspond to successful cases listed in Table 2. (A colour figure is available in the online version.)

to require different slope values in order to get the best fit. Later research also confirmed this requirement (Fraser et al. 2014; Adams et al. 2014). As a reference,  $q_L$  values estimated by Petit et al. (2011) are  $5_{-1.0}^{+1.5}$  and  $7_{-1.5}^{+1.0}$  for the hot and cold MCB populations, respectively.

The main difference between the two most successful initial SFDs (NV16 and NV19) lies in their behaviour at sizes smaller than 20 km. Around that size, the two distributions diverge, leading the NV16 SFD to have about two orders of magnitude more 1 km bodies than the NV19 SFD. The difference grows up to three orders of magnitude at 100 m. Instead, both SFDs have a similar number of bodies at sizes larger than several tens of km (Fig. 2). Fig. 7 shows that each initial SFD imprints different features in the final distribution of bodies smaller than 100 km. All final distributions in Fig. 7 correspond to runs with  $t_i = 5$  Myr. Nevertheless, the features

mentioned below are maintained even when the onset of dynamical instability is delayed by up to 30 Myr, allowing for more collisional evolution. Generally, runs starting with the NV16 SFD show a clear break at 100 km, transitioning to a shallower slope for small bodies, eventually reaching close to steady-state SFD at small sizes. Instead, runs starting with the NV19 SFD keep the initial rounded shape at sizes around 100 km.

A sizeable difference of about one order of magnitude is produced in the number of bodies smaller than about 1 km, depending on the initial SFD, and – in general – despite of the adopted power law. In the case of the NV16 initial SFD (the left-hand panel in Fig. 7), collisional evolution does not substantially change the initial SFD slope in the 100 m to 100 km size range, and dynamical depletion takes place from there. In the case of the NV19 initial SFD (the right-hand panel in Fig. 7), its shallower slope, with respect to NV16,



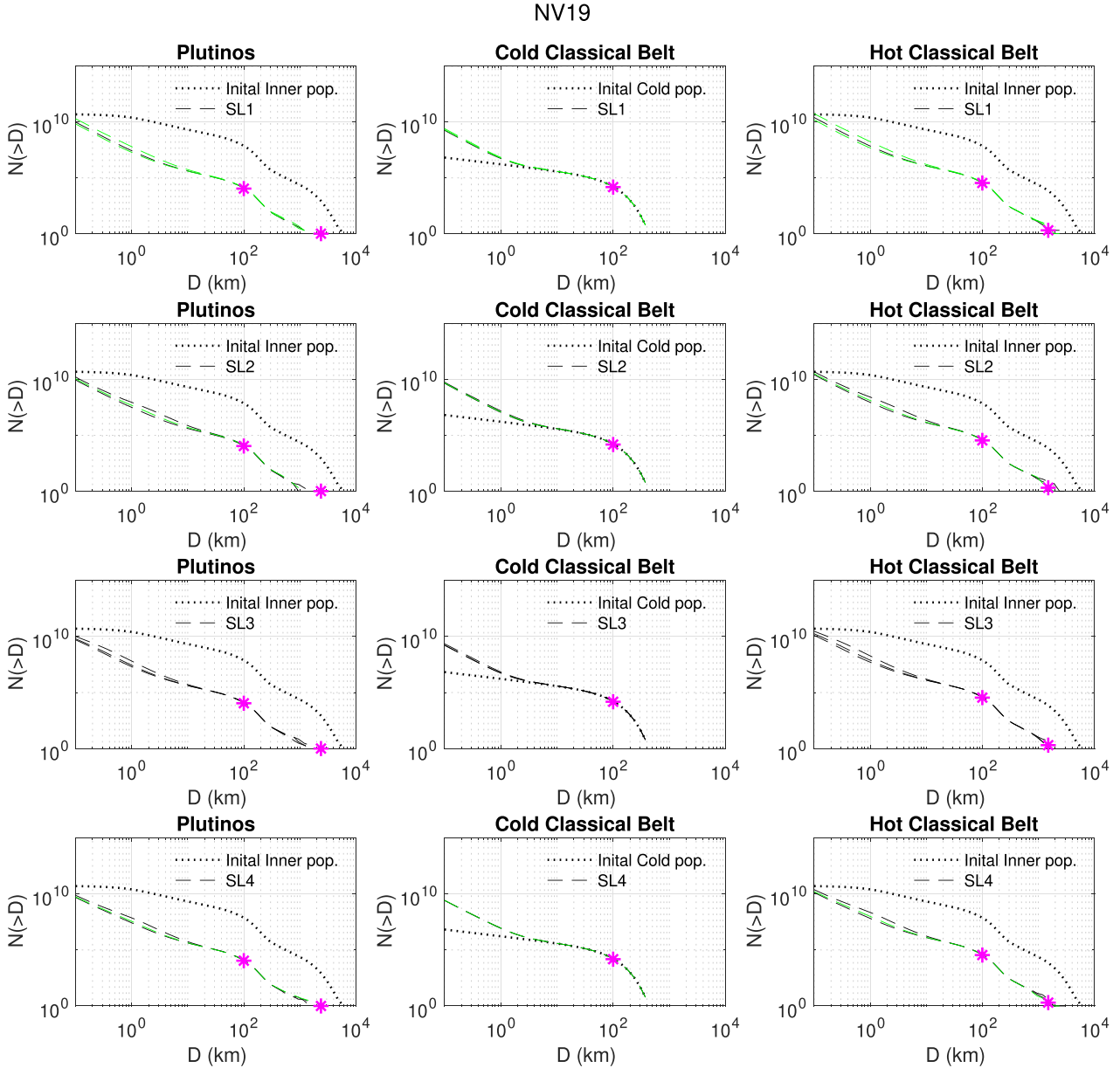


**Figure 4.** Same as Fig. 3, but with initial NV19 SFD.

leaves its print in the final distribution as a dip in the  $\sim 1\text{--}10$  km size range. Collisional evolution is just able to drive the SFD of sub-km size bodies close to equilibrium.

Minor differences between evolved populations, corresponding to any NV16 and NV19 SFDs, are due to different scaling laws, as colour dashed lines show in Fig. 7 (left-hand and right-hand panels). Differences are most noticeable in the case of SL1 and SL4 scaling laws, but only in the NV16 case. Bodies in this size-range ( $\sim 100$  m – 2 km) are mostly eroded from the original SFD, whereas in the NV19 case, they are mostly produced from the break-up of larger bodies. The role played by scaling laws is clear in this case; in fact, disruption of targets of a given size  $D$  depends on the  $Q_D^*$  value (NV16 cases), but the slope of the SFD of the generated fragments at size  $D$  does not (NV19 cases).

The analysis of the final distributions shows that collisional equilibrium is not set in the overall distribution due to the short

collisional evolution time for two reasons: (1) the two cases differ only by the initial SFDs, while at collisional equilibrium, the memory of the original SFD should have been erased; and (2) different final SFDs at different scaling laws starting with the same NV16 SFD are reached.

From these results it is apparent that Neptune’s early migration combined with few small bodies may couple to shape a smooth transition size range in the SFD between  $\sim 10$  and 100 km. Such transition region was also found by CBB12 when they considered a BPL with a shallow slope at small sizes. In that case the late dynamical instability froze the population distribution before collisional grinding could dwell the 30–100 km size range of bodies.

In summary, we find that current estimates of population abundances can be met by ALICANDEP-22 in the framework of an early dynamical instability, provided that mass depletion and transference of bodies to outer zones are suitably accounted for.

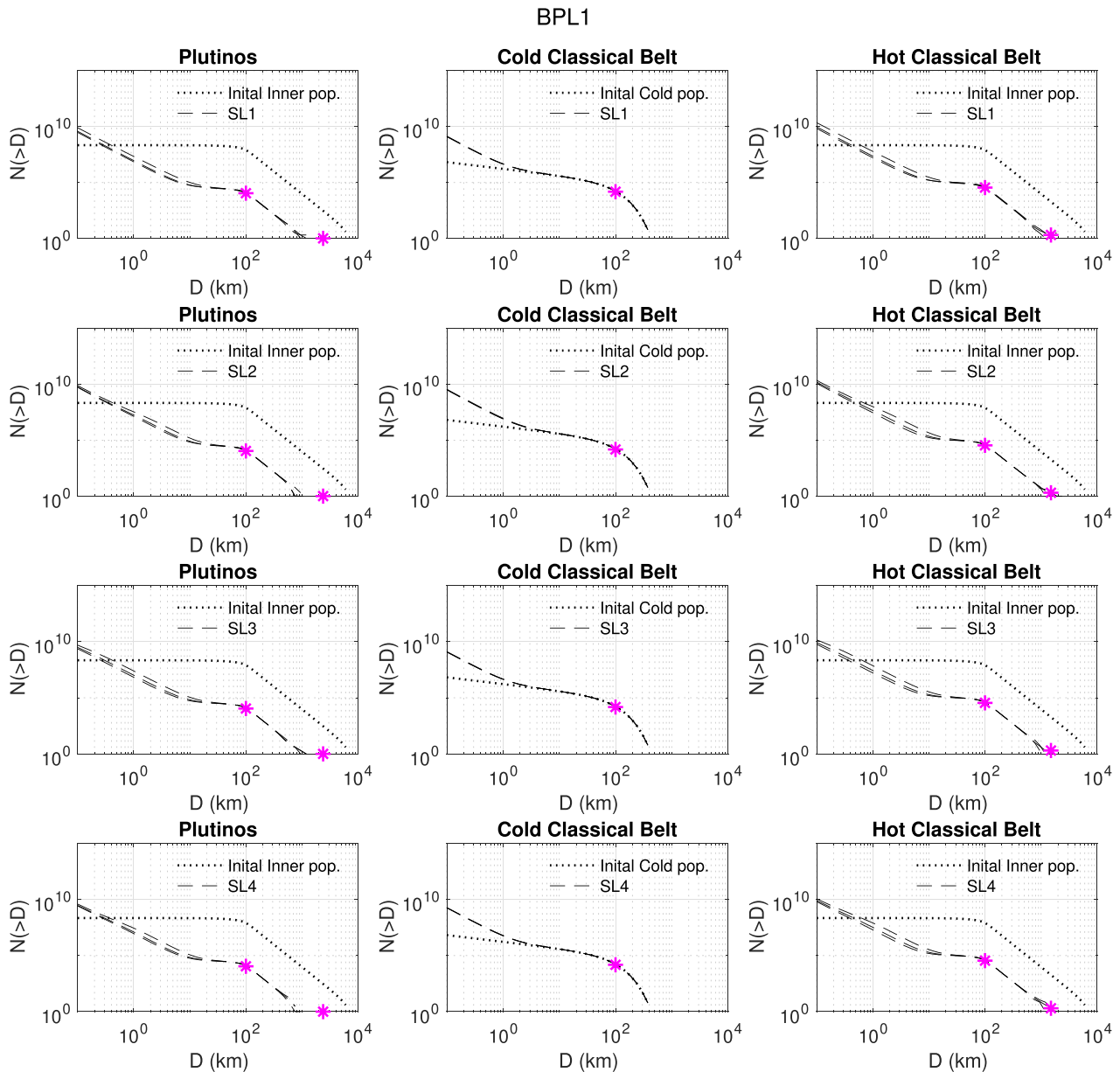


**Figure 5.** Same as Fig. 3, but with initial BPL1.

### 3.2 Mass evolution

Fig. 8 shows the time mass evolution for some of our best runs corresponding to different onset and duration of the instability phase. Plots only show the evolution for the first 50 Myr to focus on changes around the instability phase (no further change happens once dynamical instability is over). The left-hand side panel shows mass relative to initial ( $M(t)/M_0$ ) as a function of time, and the right-hand panel shows the fraction of mass depleted by dynamical effects. The most successful cases starting with the NV16 SFD need to deplete 87.9–99.1 per cent dynamically, whereas those starting with the NV19 SFD need to deplete 99.1–99.9 per cent, in order to match current observables. Therefore, provided NV19 SFD has fewer small bodies in their initial distribution than NV16, collisional evolution is less severe than in the case of an initial NV16 SFD, requiring thus more intense dynamical mass depletion.

Table 2 provides the final mass in each zone for each successful case. The mass range obtained for Zone 3 is in reasonable agreement with the mass estimated for HCs by Fraser et al. (2014) and with the estimation provided by the dynamical model of Nesvorný & Vokrouhlický (2016). Table 2 also provides the mass fraction implanted in Zones 1 and 3 with respect to the original mass. In all runs, this mass fraction is in the range of  $(1.46–2.28) \times 10^{-4}$  for Zone 1 and  $(4.75–9.35) \times 10^{-4}$  for Zone 3. This is equivalent to an implanted mass fraction in Zone 3 with respect to Zone 1, ranging from 2 to 4.2. Nevertheless, for the most successful cases in Table 2 this ratio is between 2.3 and 3.6, well within the 2–4 range predicted by observations for the ratio of bodies in the HC to the plutinos populations (CEFPS). The mass implanted in the plutinos and HC populations in our model is of the same order of magnitude as the capture statistics provided by Nesvorný & Vokrouhlický (2016).

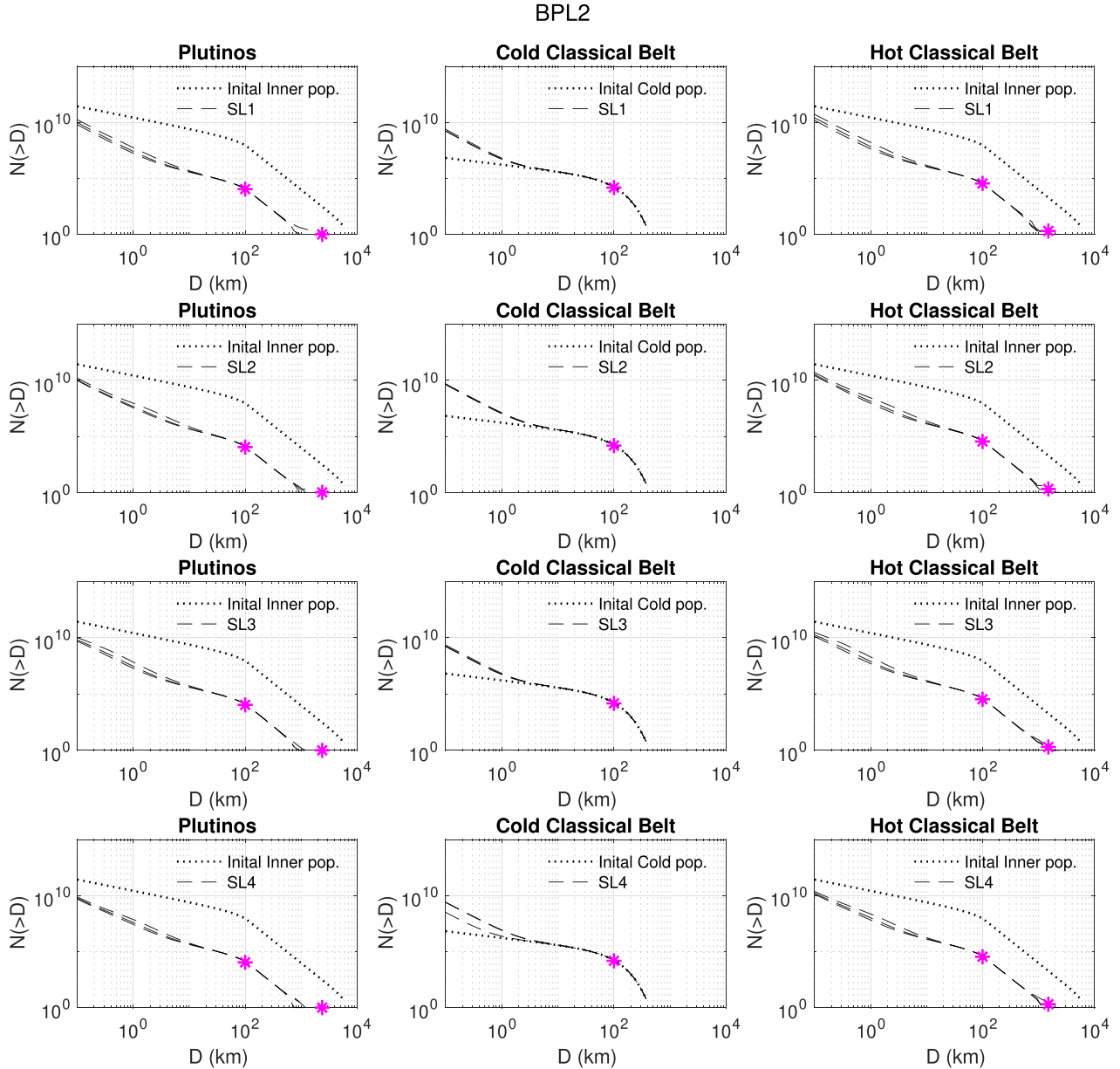


**Figure 6.** Same as Fig. 3, but with initial BPL2.

Regarding the effect of scaling law, SL2 is the one that allows for largest collisional grinding, with mass-loss up to 12 per cent of the initial mass due to collisional comminution, provided that an initial SFD has enough mass in small bodies (i.e. NV16 SFD). NV19 SFD does not reach the same degree of collisional activity due to a lack of small bodies. The short duration of the collisional regime partly feeds the small body population, but then there is no time for such a population to produce a significant collisional cascade. Finally, runs beginning with BPL1 and BPL2 SFD have similar behaviour to those with initial NV19 SFD, as both have little mass at small body sizes.

### 3.3 Origin of 67P/Churyumov–Gerasimenko and (486958) Arrokoth

In this section, we focus on the problem of the origin of comet 67P/C-G and TNO Arrokoth as primordial bodies versus gravitational aggregates. A primordial origin is favoured when the probability

is high for a body, in a given size range, not to be a collisional fragment nor a gravitational aggregate (GA).

In order to do that, for each size range corresponding to both bodies, we keep track of the primordial, re-accumulated (GA) and fragments history. It has been proposed that 67P/C-G was born in a massive inner belt and then scattered to the outer belt along with the instability (where it becomes a comet); therefore, we placed it in the Inner Zone at the beginning. The corresponding size range for 67P/C-G is 2.4–5 km. Instead, we placed Arrokoth in Zone 2, as it was put forwards that this body always belonged to the CC. The equivalent estimated size is around 18 km.

According to definitions in ALICANDEP-22 model, a primordial body is staying forever – unshattered – in the zone where it began its evolution and has only suffered cratering collisions. The definition of re-accumulated object (GA) was given in Section 2.1 as the remnant of a shattering collision with less than 50 per cent of the mass in the largest fragment. Instead, we consider a fragment as a body that is

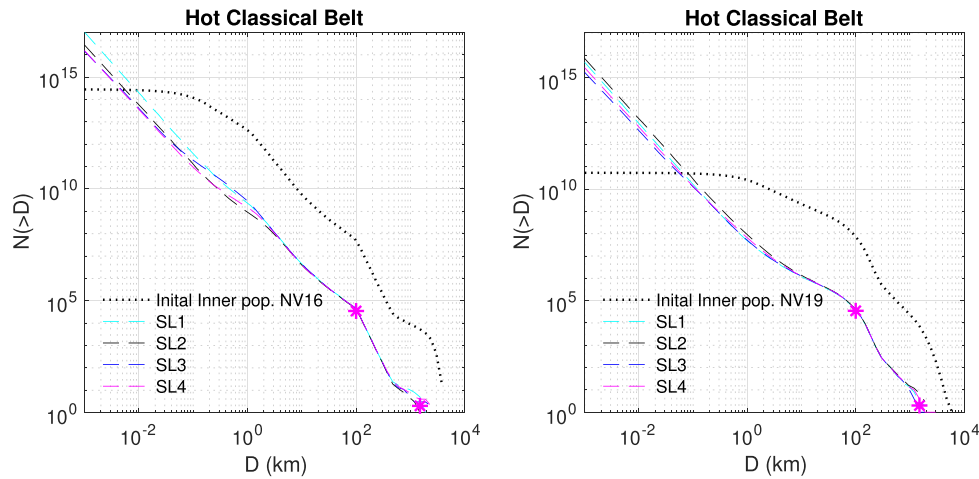


**Figure 7.** Cumulative final size-frequency distributions (SFD) of HC population as affected by different scaling laws. The panel on the left corresponds to initial NV16 SFD and the panel on the right corresponds to initial NV19 SFD. Comparison with same initial conditions for instability onset are shown ( $t_i = 5$ ). (A colour figure is available in the online version.)

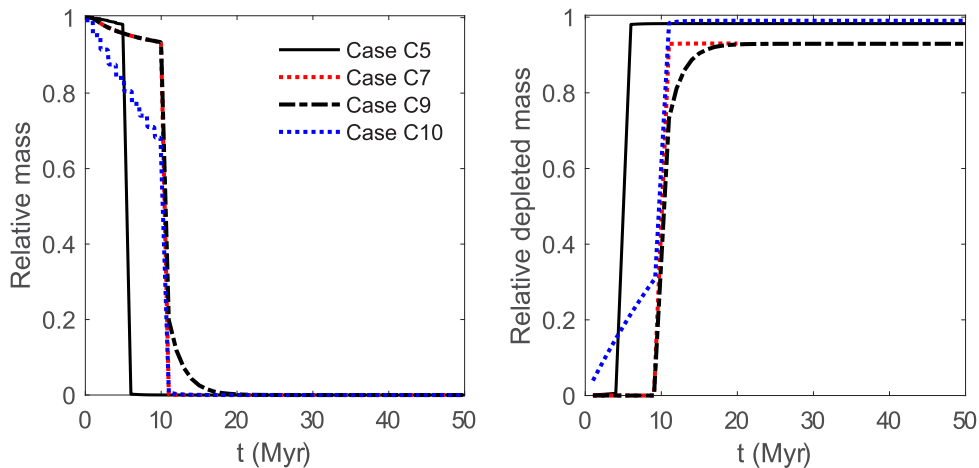


**Figure 8.** Mass evolution for representative successful runs. The left-hand panel shows mass relative to initial ( $M(t)/M_0$ ), and the right-hand panel shows the fraction of depleted mass as a function of time. The represented cases correspond to C5 (SFD: NV16, SL3,  $t_i = 5$  Myr,  $\Delta t = 10$  Myr); C7 (SFD: NV16, SL4,  $t_i = 10$  Myr,  $\Delta t = 10$  Myr); C9 (SFD: NV16, SL4,  $t_i = 10$  Myr,  $\Delta t = 30$  Myr); and C10 (SFD: NV19, SL3,  $t_i = 10$  Myr,  $\Delta t = 10$  Myr).

not a GA: it is worth mentioning that this includes all products of a shattering or cratering collision, except GA. Therefore, not only single fragments are included. In many cases, an aggregate for which the largest component mass is larger than half the whole body mass does not accomplish the definition of GA and is therefore considered a fragment.

At the beginning of simulation, both proto-67P/C-G and Arrokoth bodies belong to the ‘primordial’ category. Figs 9 and 10 show the fraction of primordial, re-accumulated and fragment bodies relative to the population at each time for successful cases indicated in Table 2, respectively, for 67P/C-G and Arrokoth. We represent those results in five panels, one per scaling law, except for SL4, which is split into two for the sake of clarity of representation. Notice that Figs 9 and 10 display different time spans. The output for 67P/C-G is shown from the beginning of the simulation until the end of the instability phase. After that time, the Inner Zone is fully depleted, and 67P/C-G would be ejected outside the region so that it undergoes no further collisional evolution. In the case of Arrokoth, we represent the outcome during the whole time span since this body is expected to remain during all its life in the same dynamical zone.

### 3.3.1 Comet 67P/C-G

Model results show that once the dynamical instability begins, the fraction of primordial bodies and fragments in the size range of 2–5 km barely change, while the fraction of re-accumulated bodies in this size range is negligible in all cases. The volume fraction of the largest component of comet 67P/C-G as of today is about 73 per cent of the overall comet volume. Such a body is classified in our model as a ‘fragment’ as it does not accomplish our definition of GA. Therefore, only a comparison between primordial and fragment bodies is made.

More in detail, scaling laws SL1 and SL3 (both corresponding to ‘strong’ bodies in the gravity regime) combined with NV16 SFD begin the instability phase with 87 per cent primordial bodies in the case it starts at 5 Myr (cases C1 and C5). Primordial body fraction drops to 45 per cent in the case the onset of instability is delayed to 30 Myr (C6). The fraction of fragments in this size range grows steadily up to 58 per cent (case C6) until instability begins. Choosing NV19 as the initial SFD, instability begins with 64 per cent primordial bodies (case C2).



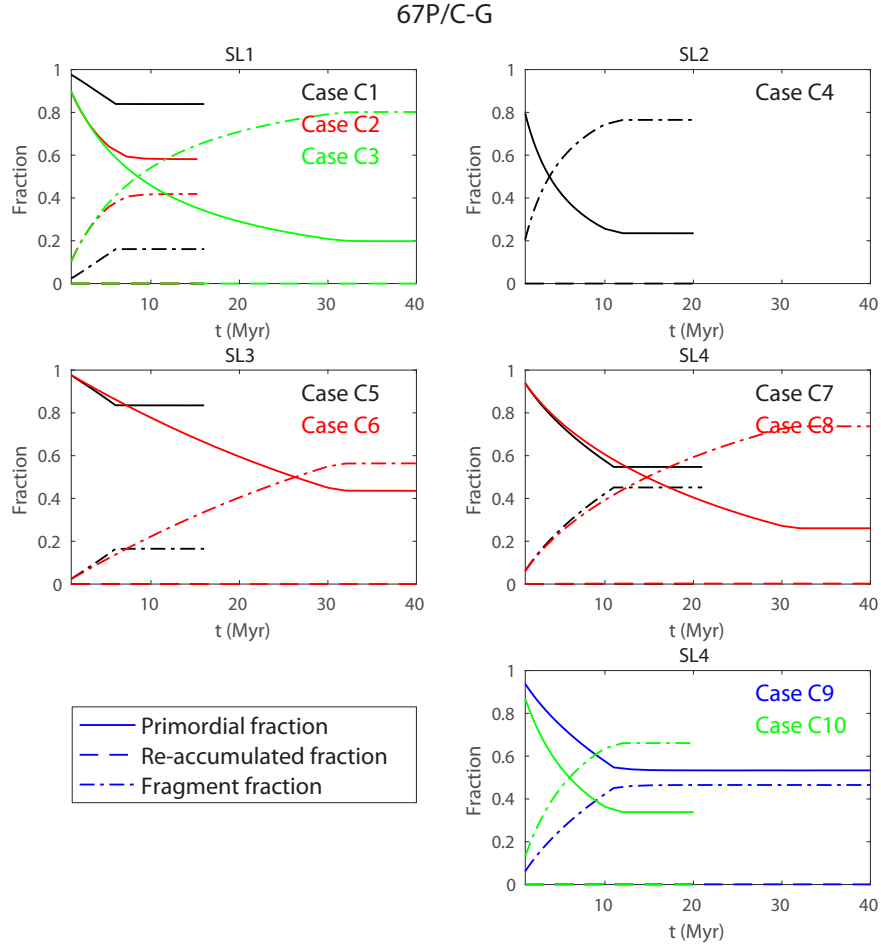


**Figure 9.** Fraction of primordial, re-accumulated bodies, and fragments for the size range corresponding to 67P/C-G, under the early giant planet instability scenario assumed in this work. (A colour figure is available in the online version.)

In the case of SL2 and SL4 scaling laws (‘weak’ bodies in the gravity regime), the instability phase is reached with a higher proportion of primordial fragments than in the case of strong bodies. For initial NV16 SFD,  $\sim 45$  per cent end as fragments in cases C7, C8, and C9 (and  $\sim 55$  per cent as primordial bodies). For SL2 and SL4 scaling laws combined with initial NV19 SFD, 66–76 per cent end as fragments for cases C4 and C10, respectively (and 24–34 per cent as primordial). Run C10 reaches  $\sim 65$  per cent of fragments by the end of the instability.

In summary, results suggest that the origin of 67P/C-G seems to depend on the adopted scaling law and initial conditions. This object may be a primordial body in the case of the BA99 scaling law and NV16 initial distribution. These conditions are favoured in case the instability occurs above 5 Myr. Instead, the possibility that 67P/C-G is the product of a collision seems to be favoured if the initial size distribution were NV19 and the scaling law in the gravity regime is of the kind proposed by LS09. Under such conditions, the probability that 67P/C-G is a collisional fragment increases up to 76 per cent, provided dynamical instability started around 5–10 Myr. This outcome is also possible in the case of initial NV16 size distribution with large weak bodies, but the instability onset was started somewhat later, around 30 Myr.

### 3.3.2 *Trans-Neptunian Object Arrokoth*

The volume fraction of the largest component of Arrokoth as of today is about 65 per cent of this TNO overall volume. Such a body is classified in the model as a primordial body or a fragment, as it does not accomplish the requirement to be a GA.

ALICANDEP-22 finds that up to 95 per cent of primordial bodies may survive in the CC in the case of an early dynamical instability scenario. In particular, the fraction of primordial bodies in the 15–23 km size range only decreases slowly and monotonously down to 95 per cent. The rate of shattering of primordial bodies shows a very subtle change in slope for the different scaling laws considered. SL1 and SL3 retain more primordial bodies than SL2 and SL4. All in all, we can say that a primordial origin of Arrokoth is the most likely (at least 95 per cent) by far under the considered evolution scenarios.

### 3.4 Pluto to Mars-size bodies in the original population

As described in Section 2, the model evolves a population of bodies up to a maximum size of 6000 km. That implies some 300 (BPL), 700 (NV19) to 2000 (NV16) Pluto-size bodies or larger in the initial population.

**Table 2.** Successful runs meeting observational constraints. The first column indicates the case label. The next four columns indicate the initial conditions used in the simulations: SL stands for ‘Scaling Law’,  $t_i$  is the start time for instability, and  $\Delta t$  is the time that lasts. Following columns indicate the results obtained for each zone, indicated in column six.  $N(>100\text{ km})$  is the number of bodies larger than 100 km,  $M_f$  is the final mass in Earth mass,  $\frac{M_{\text{impl}}}{M_0}$  is the mass implanted in zones 1 and 3 relative to the initial mass,  $q_L$  is the slope index in the final differential SFD at the large end (100–400 km), and DP indicates the average number of dwarf planets. The last row summarizes current constraints.

| Case                | SL  | Initial SFD | $t_i$<br>(Myr) | $\Delta t$<br>(Myr) | Zone     | $N(>100\text{ km})$ | $M_f (M_\oplus)$ | $\frac{M_{\text{impl}}}{M_0} (\times 10^{-4})$ | $q_L$                         | DP  |
|---------------------|-----|-------------|----------------|---------------------|----------|---------------------|------------------|--|-------------------------------|-----|
| C1                  | SL1 | NV16        | 5              | 10                  | 1        | 11 939              | 0.006            | 2.7  | 6.1                           | 0.4 |
|                     |     |             |                |                     | 2        | 14 874              | 0.005            | –  | 6.9                           | –   |
|                     |     |             |                |                     | 3        | 35 927              | 0.016            | 7.5  | 6.0                           | 2.0 |
| C2                  | SL1 | NV19        | 5              | 10                  | 1        | 11 137              | 0.004            | 1.5  | 6.1                           | 1.1 |
|                     |     |             |                |                     | 2        | 14 880              | 0.005            | –  | 6.9                           | –   |
|                     |     |             |                |                     | 3        | 33 521              | 0.015            | 5.0  | 5.9                           | 1.7 |
| C3                  | SL1 | NV19        | 30             | 10                  | 1        | 11 819              | 0.006            | 2.0  | 5.9                           | 0.7 |
|                     |     |             |                |                     | 2        | 14 878              | 0.005            | –  | 6.9                           | –   |
|                     |     |             |                |                     | 3        | 35 587              | 0.017            | 5.7  | 5.9                           | 1.6 |
| C4                  | SL2 | NV19        | 10             | 10                  | 1        | 11 276              | 0.004            | 1.5  | 5.9                           | 1.0 |
|                     |     |             |                |                     | 2        | 14 830              | 0.005            | –  | 6.9                           | –   |
|                     |     |             |                |                     | 3        | 34 822              | 0.015            | 5.1  | 5.9                           | 2.0 |
| C5                  | SL3 | NV16        | 5              | 10                  | 1        | 11 909              | 0.005            | 2.2  | 6.0                           | 0.6 |
|                     |     |             |                |                     | 2        | 14 885              | 0.005            | –  | 6.9                           | –   |
|                     |     |             |                |                     | 3        | 35 805              | 0.016            | 7.8  | 6.0                           | 1.9 |
| C6                  | SL3 | NV16        | 30             | 10                  | 1        | 11 065              | 0.005            | 2.4  | 5.9                           | 0.7 |
|                     |     |             |                |                     | 2        | 14 877              | 0.005            | –  | 6.9                           | –   |
|                     |     |             |                |                     | 3        | 35 640              | 0.017            | 8.3  | 6.0                           | 2.0 |
| C7                  | SL4 | NV16        | 10             | 10                  | 1        | 11 649              | 0.006            | 2.8  | 6.0                           | 1.0 |
|                     |     |             |                |                     | 2        | 14 855              | 0.005            | –  | 6.9                           | –   |
|                     |     |             |                |                     | 3        | 35 068              | 0.017            | 8.3  | 6.0                           | 1.3 |
| C8                  | SL4 | NV16        | 30             | 10                  | 1        | 11 346              | 0.005            | 2.4  | 6.0                           | 1.1 |
|                     |     |             |                |                     | 2        | 14 853              | 0.005            | –  | 6.9                           | –   |
|                     |     |             |                |                     | 3        | 34 953              | 0.015            | 7.3  | 6.0                           | 2.1 |
| C9                  | SL4 | NV16        | 10             | 30                  | 1        | 11 616              | 0.006            | 2.8  | 6.2                           | 1.3 |
|                     |     |             |                |                     | 2        | 14 857              | 0.005            | –  | 6.9                           | –   |
|                     |     |             |                |                     | 3        | 35 998              | 0.018            | 8.4  | 6.1                           | 2.3 |
| C10                 | SL4 | NV19        | 10             | 10                  | 1        | 10 598              | 0.006            | 2.1  | 5.9                           | 1.0 |
|                     |     |             |                |                     | 2        | 14 856              | 0.005            | –  | 6.9                           | –   |
|                     |     |             |                |                     | 3        | 34 385              | 0.015            | 4.9  | 5.9                           | 1.6 |
| Current estimations |     |             |                |                     | Plutinos | 8000–13 000         | –                | –  | $5.5^{+1.2}_{-2.4} (*^{1,2})$ | 1   |
|                     |     |             |                |                     | CC       | ~15 000             | 0.003–0.006      | –  | $8.2 \pm 1.5 (*^3)$           | –   |
|                     |     |             |                |                     | HC       | ~35 000             | 0.008–0.012      | –  | $5.3^{+0.4}_{-1} (*^3)$       | 2   |

\*<sup>1</sup> Alexandersen et al. (2016).

\*<sup>2</sup> Volk et al. (2016).

\*<sup>3</sup> Fraser et al. (2014).

Therefore, considering the successful cases reproducing current observables (all corresponding to NV16 and NV19), there might have been some 700–1900 bodies larger than Pluto up to Mars size, in the NV19 and NV16 initial mass distribution, respectively. None of them was shattered by collisional evolution, which means that they were dynamically scattered to the Outer Belt, the Oort cloud or ejected from the Solar system. Only a few of them may have been captured as satellites of the giant planets or impacting them. We may speculate that some of those objects, including a handful of bodies larger than 4000 km (and 1 Mars-size body), may currently be at a heliocentric distance such that suitable surveys can detect them. Further dynamical analysis of the evolution of scattered large bodies is needed, though, in order to make suitable predictions on their actual presence at such distance.

#### 4 DISCUSSION AND CONCLUSIONS

We have deeply modified our previous model of the collisional and dynamical evolution of the primordial region of the outer Solar

system (ALICANDEP, in CBB12). The main goal was to suitably take into account the onset of an early dynamical instability as put forward in the last decade as improvement to the Nice model. The new model (ALICANDEP-22) considers an original region containing 20–30  $M_\oplus$  from which bodies are either dynamically ejected from the region or implanted in two zones corresponding to the current plutinos and hot classical trans-Neptunian belt. In addition, an *in situ* population of objects is present since the beginning, corresponding to the current cold-classicals. Collisional and dynamical evolution is allowed starting from initial conditions proposed in recent literature. We summarize and discuss here the main results obtained by ALICANDEP-22:

(1) We identified sets of boundary conditions for the collisional and dynamical evolution of the primordial outer disc for which ALICANDEP-22 matches main current observables (Table 2). All successful runs correspond to the initial SFDs identified as NV16 and NV19.

(2) The currently estimated number of bodies larger than 100 km in each region of the TB is matched fairly well.

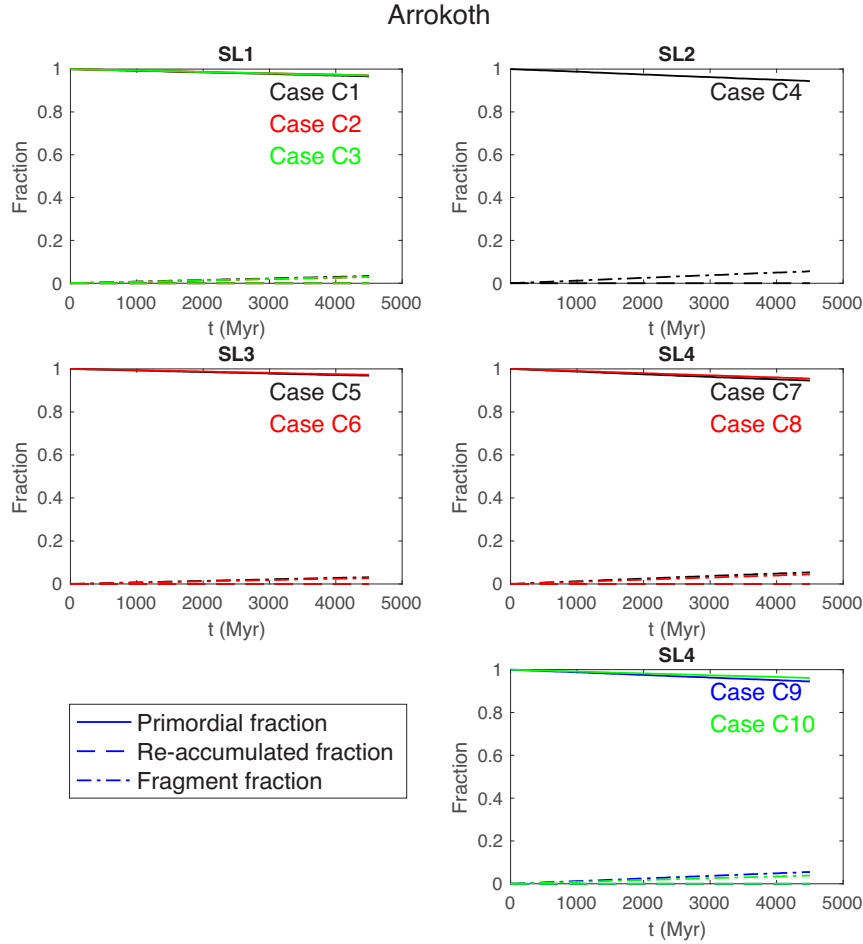


**Figure 10.** Fraction of primordial, re-accumulated bodies and fragments for the size range corresponding to Arrokoth-size body in Zone 2 under the early giant planet instability scenario assumed in this work. (A colour figure is available in the on-line version.)

(3) Dwarf planets observed in the plutinos and hot classical TNO populations are suitably reproduced by the model. An average number of 0.9 bodies larger than 1800 km are found in the plutinos population and 1.8 bodies the size of Makemake and Haumea dwarf planets are found. Our model allows for a Poisson probability of 0.85 of having at least one undiscovered large body in the outskirts of the HC population.

(4) Features proposed recently in the SFD in the multi-km size range ( $D > 4$  km) and those corresponding to the different dynamical populations can be reproduced reasonably well by our model.

(5) The lack of bodies larger than 400 km in the cold classical population of TNOs is an automatic finding as none of the starting CC populations contain such bodies.

From reported results, we may summarize that collisional evolution is relatively soft when dynamical instability starts early, before 30 Myr, in a primordial disc of  $20\text{--}30 M_{\oplus}$ . In this case, the only change to the initial shape of the distribution regards the slope of the SFD for bodies  $D < 10$  km. This result implies the following:

(1) The initial size distribution of bodies smaller than 10 km largely affects the shape of the evolved SFD and the amount of bodies smaller than 20–30 km.

(2) The initial shape of the SFD (not the absolute number of bodies) for large bodies ( $D > 10$  km) is not significantly affected by collisional evolution. Thus, the population of bodies larger than

10 km is only reduced according to dynamical depletion without modifying its primordial shape distribution.

(3) Initially rounded populations around  $\sim 100$  km, followed by shallow slope at largest bodies end (Pluto-size) – such as NV16 and NV19 – are more likely to end evolution with the required number of dwarf planets observed in the plutino and HC populations, compared to a primordial BPL.

(4) The SFD of the implanted populations (plutinos and HC) recalls the shape of the SFD of the observed population of Jupiter Trojans (in the comparable size range). Among the distributions studied in this work, the NV16 SFD is the one that achieves a better agreement with that population in a greater size range (4–100 km), compared to NV19.

The results of this work rule out the possibility that primordial population is suitably represented by some kind of BPL distribution. That is due to the difficulty of this type of SFD to simultaneously reproduce the expected number of bodies with  $D > 100$  km and the dwarf planets observed in the population of plutinos and HC. In addition, collisional evolution is essentially stopped once dynamical instability phase begins, preventing a gradual change of the SFD around 100 km, which is instead present in the population of Jupiter’s Trojans.

Dynamical simulations of the inner disc dispersion during the giant planet instability show that the implantation probability in

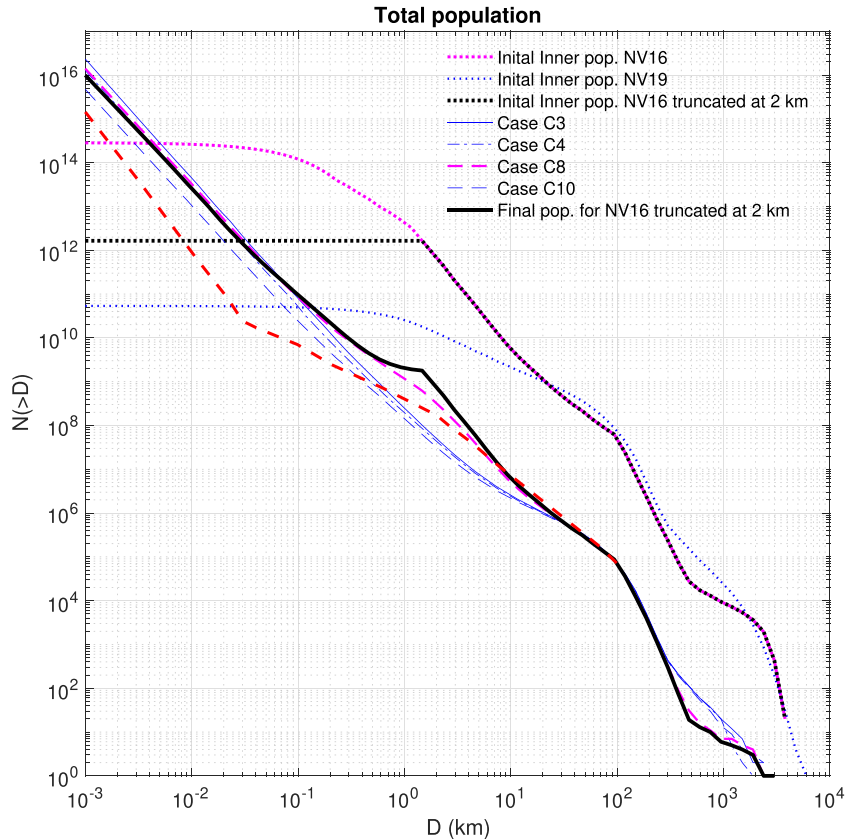


**Figure 11.** Cumulative final size-frequency distributions for all trans-Neptunian objects. The dashed red line is the reconstructed SFD from Morbidelli et al. (2021). The dashed black line is the NV16 initial SFD truncated around 2 km, and the solid black line is the evolved corresponding population. (A colour figure is available in the online version.)

different parts of the Kuiper Belt is expected to be  $10^{-3}$ – $10^{-4}$  (Nesvorný & Vokrouhlický 2016). Thus, these models imply that more than 99 per cent of the primordial mass has been depleted. Our results show that the mass fraction implanted in the populations of plutinos and HCs are of the same order of magnitude as the capture probabilities for these populations estimated by Nesvorný & Vokrouhlický (2016) in their grainy migration cases. In addition, we obtain that the ratio between the implanted mass in the hot and in the plutinos populations is within the observational estimated range of 2–4. Furthermore, our successful cases require that – in order to meet observational constraints – a dynamical mass depletion between 90 and 99.9 per cent of the primordial disc is required.

Regarding the cold population, our results show that the collisional evolution in this region is negligible, and very little mass is lost by collisional grinding. However, it is enough to modify the slope of the SFD for bodies smaller than a few kilometres, reaching a steady-state slope  $q \sim 3$ – $3.5$  for this size range. Bodies larger than a few km very rarely undergo shattering collisions. Our results show that more than 99.9 per cent of the  $D > 100$  km bodies in the CC are primordial. Comparison with available estimates of the slopes of the high size end of populations reported in Table 2 should be made with caution. In fact, model estimates are performed for the 100–400 km size range, which is the smooth part of the distribution for large bodies. Instead, current observational estimates run from some 100 km up to the whole size range of large TNOs.

It is interesting to compare ALICANDEP-22 results with the overall SFD population of the trans-Neptunian belt reconstructed by M21 (Fig. 11). They included several observational constraints

such as the abundance of dust from the New Horizons mission (NASA) estimation at hundreds of  $\mu\text{m}$ , Arrokoth cratering record, the calibration of Pluto cratering record, the SFD slope of the Trojan population, and the total number of bodies with  $D > 100$  km. We compared the final SFD of the overall population obtained in representative ALICANDEP-22 successful cases (Table 2) with such reconstructed SFD from M21, as shown in Fig. 11. Satisfactory agreement to the M21 SFD is found for runs C5, C8, and C9, corresponding to the NV16 initial SFD, especially in the range of  $\sim 2$ – $100$  km. Case C3, C4, and C10, starting with the NV19 SFD, also shows an acceptable match, limited to  $D > 20$  km. Agreement in this size range is important because it corresponds to the size range estimated from the Jupiter Trojans population, which is well constrained above 10 km. Instead, no agreement is found in the 0.03–2 km size range with the M21 distribution, which is shallow ( $q = 2.2$ ) compared to other size ranges. M21 also suggested a minimum in the scaling law at  $\sim 30$  m (SL3) to match their estimated slope in that size range. Our results do not show a related feature in the final SFD. Nevertheless, we are neutral on the presence of such a minimum because when collisional evolution is limited in time, the effect of such features in scaling law have not enough time to produce a measurable effect on the evolved SFD.

However, to try and explain the mismatch at  $\sim 30$  m, we performed several extra runs focussing on this issue. On the one hand, we postponed the instability onset to 50 and 100 Myr, in the case of initial NV16 SFD with LS3 and LS4. This did not result in the expected outcome on evolved SFD. On the other hand, the behaviour of the M21 distribution looks somewhat characteristic



of a frozen collisional cascade from a SFD with negligible mass below some size (see CBB12). For that reason, we advanced the onset of instability, reducing collisional evolution to just 1 Myr with little mass below 1 km. In this case, the final size distribution shows some trend to follow the shallow power-law indicated by M21 below 1 km, but it departs from it at a few hundred meters. The elbow at 30 m cannot be reproduced by our model; nevertheless, the average slope in the 200 m to 2 km size range matches the corresponding M21 distribution (see Fig. 11, ‘truncated’ NV16 initial SFD). However, the short duration of collisional evolution (1 Myr) in this case preserves up to one order of magnitude more 1 km-size bodies than in the case of later onset of the instability.

It is well known that ‘wavy’ size distributions may arise in collisional evolution and are responsible for modulated changes in slope, provided abrupt or even smooth cutoff is present at the small end of size distributions (Campo Bagatin et al. 1994). Such a cut-off is normally considered artificial, so collisional evolution models (like ALICANDEP-22) use an artificial tail distribution preventing wavy behaviour to show up. However, a low end of the distribution must be present at some small size ( $D < 1$  cm). We plan to address the study of the implication of relaxing the low-end tail condition on the evolved SFD. Such effect, combined with an early instability freezing collisional evolution, might trigger some wavy pattern that may appear in the size distribution faster than in the case of a minimum in the scaling law at 30 m (which is otherwise not further supported by experimental nor theoretical study so far).

ALICANDEP-22 cases matching current observables are particularly suitable for checking the collisional history of bodies at given size ranges, as comet 67P/C-G and TNO Arrokoth. The debate on their potential primordial origin led us to apply our model to such bodies.

The probability of a primordial origin for comet 67P/C-G is highest (80 per cent) when the initial conditions are set to NV16, the onset of instability happens early (5 Myr), and high specific energy for shattering is required (SL1 or SL3). This conclusion is partly supported by an analysis of the *Rosetta* (ESA) mission data which shows that the current components of this body (i.e. the two lobes) are relatively unprocessed and may have retained primordial features such as the layering reported by Massironi et al. (2015). On the contrary, such probability falls to 20–30 per cent for NV19 initial conditions and a later onset of dynamical instability (10–30 Myr) is assumed, together with low specific energy for shattering (SL2 or SL4). This is quite expected as the latter boundary conditions allow for more collisional evolution. These results are in agreement with Morbidelli & Rickman (2015) supporting that 67P/C-G is likely a collisionally evolved object rather than a primordial body formed in the inner belt and scattered outward during dynamical instability. Numerical studies support the possibility to form a body with a bi-lobed shape by shattering a suitable parent body. For example, Jutzi & Benz (2017) showed that 67P/C-G could result from sub-catastrophic collisions or even be produced by shape-changing impacts (Jutzi et al. 2017). Besides, Jutzi et al. (2017) suggest that any bi-lobed structure (including 67P/C-G) could have originated in a recent event (the last 1 Gy), instead of being primordial. Later, Schwartz et al. (2018) showed that it is also possible to form elongated bodies and bi-lobed shapes under a regime of catastrophic collisions of larger bodies as the gravitational re-accumulation of the fragments. Schwartz et al. (2018) suggest that such a process can occur at any time in the history of the Solar system, so they should not be necessarily primordial. More recently, Campo Bagatin et al. (2020) showed that the formation of contact binary-like objects might be

a natural outcome of the post-impact fragment self-reaccumulation process.

Other combinations of boundary conditions lead to a relatively moderate difference between the two possible outcomes. We conclude that no definitive answer can be given by the model on the origin of the best-known comet ever.

In the case of the cold classical TNO Arrokoth, little chance is left other than primordial origin. In fact, all simulations show that the probability of such a body remaining unshattered is at least 95 per cent. The very limited collisional evolution of that region of the belt prevents objects of Arrokoth-size to be shattered.

As for the high end of the TNO population, ALICANDEP-22 predicts an average 83 per cent probability that at least another object larger than 1500 km in diameter is lurking in the outer hot classical belt. It cannot, therefore, be ruled out that such an object is currently in a particularly unlucky location preventing surveys from discovering it. For instance, an object with  $a \sim 45$  au, relatively high eccentricity  $e \approx 0.4$ – $0.4$  and high inclination  $i \approx 30^\circ$ – $40^\circ$ , may be at some 65 au heliocentric distance in a region of the sky usually not scanned by discovery surveys. Nevertheless, it should not be overlooked that – obviously – a non-negligible 17 per cent Poisson probability of having no other large in the HC applies in model results.

Finally, we find that the initial size distributions that allow ALICANDEP-22 to match current TNO region observables are compatible with the presence – at the beginning of the evolution – of bodies as large as 6000 km.

Depending on initial conditions, 25–400 objects larger than Pluto may have been present in the primordial population until the beginning of the instability phase, and a few (4–6) bodies larger than 4000 km, including one Mars-size that were dispersed during that phase to unknown destiny. Such bodies may have been ejected from the inner belt and be now stranded in the distant Solar system waiting to be discovered. Future dynamical studies and surveys in search for large bodies are called to confirm whether such a rogue planet is present at large heliocentric distance.

## ACKNOWLEDGEMENTS

PGB and ACB acknowledge funding by the Spanish Ministerio de Investigación, Ciencia e Innovación through project RTI2018-099464-B-I00 ‘Retos de la Sociedad’ (2018 call). JC acknowledge the University of Surrey and its Physics department for giving him the opportunity that allowed him to stay at the University of Alicante (UA) and to collaborate to this work during part of 2020. AAC acknowledges UA grant UATALENTO18-02 and from the State Agency for Research of the Spanish MCIU through the ‘Center of Excellence Severo Ochoa’ award to the Instituto de Astrofísica de Andalucía (SEV-2017-0709). We thank the International Space Science Institute (ISSI Bern), who supported the OCEOSS project where some of this work was discussed. We also thank the anonymous reviewer for helpful suggestions.

## DATA AVAILABILITY

Any interested reader may contact PGB to have access to the data used by the authors to derive results presented in this manuscript.

## REFERENCES

- Adams E. R., Gulbis A. A. S., Elliot J. L., Benecchi S. D., Buie M. W., Trilling D. E., Wasserman L. H., 2014, *AJ*, 148, 55

- Alexandersen M., Gladman B., Kavelaars J. J., Petit J.-M., Gwyn S. D. J., Shankman C. J., Pike R. E., 2016, *AJ*, 152, 111
- Bannister M. T. et al., 2018, *ApJS*, 236, 18
- Batygin K., Brown M. E., Fraser W. C., 2011, *ApJ*, 738, 13
- Benavidez P. G., Campo Bagatin A., 2009, *P&SS*, 57, 201 (BCB09)
- Brasser R., Morbidelli A., 2013, *Icarus*, 225, 40
- Buie M. W. et al., 2015, *AJ*, 149, 113
- Benz W., Asphaug E., 1999, *Icarus*, 142, 5 (BA99)
- Bernstein G. M., Trilling D. E., Allen R. L., Brown M. E., Holman M., Malhotra R., 2004, *AJ*, 128, 1364
- Bottke W. F., Norman M. D., 2017, *AREPS*, 45, 619
- Campo Bagatin A., Benavidez P. G., 2012, *MNRAS*, 423, 1254 (CBB12)
- Campo Bagatin A., Cellino A., Davis D. R., Farinella P., Paolicchi P., 1994, *P&SS*, 42, 1079
- Campo Bagatin A., Petit J.-M., Farinella P., 2001, *Icarus*, 149, 198
- Campo Bagatin A., Alemañ R. A., Benavidez P. G., Pérez-Molina M., Richardson D. C., 2020, *Icarus*, 339, 113603
- Dawson R. I., Murray-Clay R., 2012, *ApJ*, 750, 43
- de Sousa R. R., Morbidelli A., Raymond S. N., Izidoro A., Gomes R., Vieira Neto E., 2020, *Icarus*, 339, 113605
- Fernandez J. A., Ip W.-H., 1984, *Icarus*, 58, 109
- Fraser W. C., Brown M. E., Morbidelli A., Parker A., Batygin K., 2014, *ApJ*, 782, 100
- Fuentes C. I., Holman M. J., 2008, *AJ*, 136, 83
- Gladman B., Marsden B. G., van Laerhoven C., 2008, in Barucci A., Boehnhardt H., Cruikshank D., Morbidelli A., eds, *The Solar System Beyond Neptune*. p. 43
- Gladman B. et al., 2012, *AJ*, 144, 23
- Gomes R., 2021, *Icarus*, 357, 114121
- Gomes R., Levison H. F., Tsiganis K., Morbidelli A., 2005, *Nature*, 435, 466
- Grav T. et al., 2011, *ApJ*, 742, 40
- Hahn J. M., Malhotra R., 2005, *AJ*, 130, 2392
- Jorda L. et al., 2016, *Icarus*, 277, 257
- Jutzi M., Benz W., 2017, *A&A*, 597, A62
- Jutzi M., Benz W., Toliou A., Morbidelli A., Brasser R., 2017, *A&A*, 597, A61
- Kavelaars J. J. et al., 2009, *AJ*, 137, 4917
- Kavelaars J. J. et al., 2021, *ApJ*, 920, L28
- Leinhardt Z. M., Stewart S. T., 2009, *Icarus*, 199, 542
- Leinhardt Z. M., Stewart S. T., 2012, *ApJ*, 745, 79
- Levison H. F., Morbidelli A., van Laerhoven C., Gomes R., Tsiganis K., 2008, *Icarus*, 196, 258
- Massironi M. et al., 2015, *Nature*, 526, 402
- Morbidelli A., Rickman H., 2015, *A&A*, 583, A43
- Morbidelli A., Levison H. F., Tsiganis K., Gomes R., 2005, *Nature*, 435, 462
- Morbidelli A., Gaspar H. S., Nesvorný D., 2014, *Icar*, 232, 81
- Morbidelli A., Nesvorný D., Laurenz V., Marchi S., Rubie D. C., Elkins-Tanton L., Wieczorek M., Jacobson S., 2018, *Icarus*, 305, 262
- Morbidelli A., Nesvorný D., Bottke W. F., Marchi S., 2021, *Icarus*, 356, 114256
- Nesvorný D., 2015a, *AJ*, 150, 68
- Nesvorný D., 2015b, *AJ*, 150, 73
- Nesvorný D., 2018, *ARA&A*, 56, 137
- Nesvorný D., Vokrouhlický D., 2016, *ApJ*, 825, 94
- Nesvorný D., Vokrouhlický D., 2019, *Icarus*, 331, 49
- Nesvorný D., Vokrouhlický D., Morbidelli A., 2013, *ApJ*, 768, 45
- Nesvorný D., Vokrouhlický D., Bottke W. F., Levison H. F., 2018, *Nature Astron.*, 2, 878
- Nesvorný D. et al., 2020, *AJ*, 160, 46
- O'Brien D. P., Greenberg R., 2005, *Icarus*, 178, 179
- Petit J.-M., Farinella P., 1993, *CeMDA*, 57, 1
- Petit J.-M. et al., 2011, *AJ*, 142, 131
- Porter S. B. et al., 2018, *AJ*, 156, 20
- Schwartz S. R., Michel P., Jutzi M., Marchi S., Zhang Y., Richardson D. C., 2018, *Nature Astron.*, 2, 379
- Shankman C., Gladman B. J., Kaib N., Kavelaars J. J., Petit J. M., 2013, *ApJ*, 764, L2
- Simon J. B., Armitage P. J., Li R., Youdin A. N., 2016, *ApJ*, 822, 55
- Simon J. B., Armitage P. J., Youdin A. N., Li R., 2017, *ApJ*, 847, L12
- Singer K. N. et al., 2019, *Science*, 363, 955
- Sierks H. et al., 2015, *Science*, 347, aaa1044
- Spencer J. R. et al., 2020, *Science*, 367, aay3999
- Tsiganis K., Gomes R., Morbidelli A., Levison H. F., 2005, *Nature*, 435, 459
- Volk K. et al., 2016, *AJ*, 152, 23
- Wolff S., Dawson R. I., Murray-Clay R. A., 2012, *ApJ*, 746, 171

This paper has been typeset from a  $\text{\TeX}/\text{\LaTeX}$  file prepared by the author.